CONCENTRATED SOLAR CHEMISTRY:
DESIGN STAGE THEORETICAL THERMODYNAMIC ANALYSIS OF AN IRON-ETHYLENE PRODUCTION PROCESS

A Thesis

Presented to

The Academic Faculty

by

William Sheline

In Partial Fulfillment

of the Requirements for the Degree

Mechanical Engineering in the

School of Woodruff School of Mechanical Engineering

Georgia Institute of Technology

May 2013

CONCENTRATED SOLAR CHEMISTRY:

DESIGN STAGE THEORETICAL THERMODYNAMIC ANALYSIS

OF AN IRON-ETHYLENE PRODUCTION PROCESS

Approved by:

Dr. Sheldon Jeter, Advisor

School of Mechanical Engineering

Georgia Institute of Technology

Dr. Said Abdel-Khalik

School of Mechanical Engineering

Georgia Institute of Technology

Dr. Peter Loutzenhiser

School of Mechanical Engineering

Georgia Institute of Technology

Date Approved: April 1, 2013

ACKNOWLEDGEMENTS

I would like to thank all of my committee members for their plentiful suggestions on this project. In addition, I would like to thank Dr. Jeter for his ideas and financial support. I would like to thank my past professors at Valparaiso University (Dr. Palumbo and Dr. Duncan) as well as my parents for their moral and academic support. Finally, I appreciate all of the work and helpful feedback provided by Timothy Hurst on calculations and especially in the creation of Figures and Tables.

TABLE OF CONTENTS

LIST OF FIGURES

LIST OF TABLES

SUMMARY

Although concentrated solar power can be used to produce power using traditional electricity generation, energy storage has become a problem due to the intermittent supply of solar energy. By using solar energy in chemical production processes, the solar energy can be stored in a useful chemical product. The purpose of this thesis will be to examine the possibilities of a new solar chemical cycle the produces iron and ethylene from hematite (a form of iron oxide) and ethane using concentrated solar power. These two products are important stepping stones in the production of steel and polymers. This process could allow for the current process of steel production to move away from processes using coal and towards a more sustainable process using the hydrogen formed from the ethane cracking process and solar energy. The thesis will include: (1) the development of a new solar powered iron and ethylene combined cycle, (2) a feasibility study of a Concentrated Solar Heat Supply System (CSHSS) being developed at Georgia Tech, and (3) an assessment of the proposed cycle. The assessment will include an estimate of production including a thermodynamic ASPEN model, assessment of research to realize actualization of the theoretical cycle, an exergy analysis, and a heat exchanger analysis for the exchange of heat between the CSHSS and the chemical process.

1. Background on Concentrated Solar Technology

Although solar energy has become synonymous with photovoltaic cells due to the wide spread distribution of small scale panels, concentrated solar technologies also seek to harness solar energy by concentrating the dilute solar radiation using mirrors and optics. Contrary to the photovoltaic cells which convert sunlight directly into electricity, concentrated solar power plants generally supply high quality heat which can be used in a heat engine cycle to produce electricity or for other industrial applications. This is done through the collection, absorption, and concentration of solar radiation. The concentrated sunlight can be used in any application that requires high (or low) quality heat including electricity generation, biofuel or synthesis gas processes, or even iron production. The application of solar heat to processes other than electricity generation is important for reducing the dependence on fossil fuels caused by industrial processes. Iron production, for example, uses a direct reduction method that consumes coal releasing harmful chemicals. Industrial processes such as this iron process require an alternative renewable energy source that supplies heat rather than electricity. Concentrated solar technologies are efficient, renewable alternatives for producing this industrial heat.

Concentrated solar technologies use various means to collect and concentrate solar radiation. By collecting and concentrating sunlight, they all supply heat at various temperatures that can be used for various applications. The newest Concentrated Solar Heat Supply System (CSHSS) design, that is the only design used throughout this thesis, utilizes a Concentrated Solar Power Tower (CSPT) or central receiver design. Two other main designs exist: concentrating trough power plants and parabolic concentrator plants. The central receiver design was selected because of its high temperature capability, lower cost design, and scalability. The trough power plant design requires long lengths of pipe to increase to only marginal temperatures, and cannot achieve the high temperatures needed. The parabolic concentrators have the potential to have larger concentration ratios and reach higher temperatures, but are limited in scale and are not scalable. Each parabolic dish must generate its own products limiting the size of the individual plants. The central receiver design has a central receiver with a large field of heliostats that can be scaled to the size of plant desired. This allows plants to reach the 100 MW scale or larger while also being cost effective. The heliostats are generally only flat mirrors and do not require the elaborate manufacturing that parabolic mirrors require.

Although CSPT systems are constantly evolving, an example of a CSPT is shown in Figure 1. This figure shows the three main components of a CSPT: the heliostat field, the solar receiver, and the central tower. The heliostat field includes a field of flat mirrors that track the sun and reflect the sunlight on the solar receiver. By having thousands of heliostats reflecting sunlight on a single point, the sunlight can be concentrated several thousand times. The solar receiver is positioned at the top of the central tower in order to be able to absorb the incident sunlight from the heliostats. Due to the high intensity solar radiation supplied by the heliostat field, the solar receiver must be designed to withstand high thermal stresses and high temperatures while also having a high absorptivity and the ability to transfer heat to a heat transfer fluid. Once the solar radiation is absorbed by the solar receiver, the heat can be transferred to a heat transfer fluid such as steam, molten salts or even a particulate such as sand. This fluid can be a thermal storage medium that allows the thermal energy to be stored for later use, or it can be a working fluid that converts the thermal energy into some useful product such as

electricity or chemical products. The final component, the central tower, acts as a support structure to lift the receiver off the ground while also being a housing for various heat exchangers, turbines, pumps and other machinery necessary for the conversion of the thermal heat into electricity or other products. The interaction between the heliostat field, receiver and tower allows for the sunlight to be collected, focused on a central point, absorbed to produce heat, and leaves space for processing the heat into a useful product.

Figure 1: Concentrated Solar Power Tower

Due to 2nd law considerations, concentrated solar heat is best used for high temperature industrial applications. Although a prevalent use of the CSHSS is for electricity generation, the relatively low temperature Rankine Cycle does not take full advantage of the high temperature capabilities of the Concentrated Solar Heat. Rankine Cycles operate around 500°C while Concentrated Solar Heat reaches temperatures of 1300°C and has the potential to reach even higher temperatures as solar receiver technology is improved. This results in the loss of a large amount of work potential (exergy) which is shown later in the heat exchanger exergy analysis. A better application for the Solar Heat is in industrial applications that require heat around 1000°C. A major area of interest is in chemical process applications. This includes applications ranging from production of quicklime to hydrogen to metals such as Zn and Mg.[1,2] Many of these processes require a large amount of thermal energy for both the production and separation of chemical products. Unfortunately, the temperature and amount of heat required by each chemical process is different for every application. Some applications require large amounts of low temperature heat while others require high temperature heat while still others produce heat. This gamut of heat requirements makes it difficult to find an industrial chemical processing application that maximizes the potential of the heat supplied by the CSHSS. This exergy improvement is demonstrated later with a comparison of a Rankine cycle heat rate diagram and a heat rate diagram of the proposed chemical process (section 7).

In addition to the advantage of industrial processes increasing the exergy efficiency (decreasing lost potential work), the production of chemical or metal products eliminates the problems of intermittent supply and demand. Normally with an electric generating power plant, the supply of sunlight and the demand of

electricity are changing throughout the day. This requires large amounts of thermal storage to allow for the power plant to store thermal energy for use throughout the night and to be constantly changing generation rates to meet the changing demands of the power grid. By producing a chemical product, this problem is eliminated. The only need for energy storage is to smooth out the production rate of the chemical process which is a much smaller requirement than the requirements of storing thermal energy for 24 hour a day operation. In addition, several of these chemical products could be used as fuels which could solve the energy problem faced by the transportation sector.

2. Chemical Process Selection

The chemical selection process included finding and evaluating several possible chemical processes to determine which ones would be conducive to using concentrated solar heat in the production process. The ideal process for use with the CSHSS would require a large amount of heat to produce, would require heat at temperatures around 900°C, and would be a high value industrial product. To find the best process possible, it was important to find as many chemical processes as possible to evaluate. Then, evaluation of the processes helped determine which ones would be feasible for the process. From the remaining feasible processes, a combined iron-ethylene process was selected as the chemical process for complete thermodynamic analysis.

Several chemical processes were not feasible for use with the CSHSS. These chemical processes were mainly processes that did not require heat (i.e. exothermic) or required temperatures well beyond what solar could provide. Examples of these processes included processes to produce ammonia and tungsten. Ammonia is a chemical product used in fertilizer and many other applications and is produced at a rate of several million metric tons per year. The production of ammonia is generally done through the haber-bosch process as shown in Equation 2.1:[3]

$$3H_2 + N_2 \rightarrow 2NH_3 \tag{2.1}$$

In general, the hydrogen is produced from methane and the nitrogen is available through separation of air. Although some heat would be needed for the production of hydrogen, the reaction shown is exothermic meaning it does not require heat and thus would gain no benefit from a CSHSS. Another example of a product not currently suited for CSHSS production is Tungsten. Tungsten is a metal generally used in halogen lamps. The unique properties of tungsten include is high melting temperature, high density and high hardness. These properties make it ideal for high temperature applications from solar heat to aerospace. Tungsten would require extremely high temperatures to produce via direct decomposition or hydrogen reduction, so it is generally produced via electrolysis of its ores such as scheelite.[4] This process is similar to the process used to produce other metals. Due to the high temperatures, tungsten exceeds the planned capabilities of the CSHSS being developed at Georgia Institute of Technology, and was eliminated as a possibility; however, it does not exceed the temperature capabilities of concentrated solar power in general, and could be feasible in the future especially due to its allure as an industrial product.

Two other potential solar chemical products include the production of coke and quicklime. Coke is a product formed by the heating of coal in an oxygen-less furnace. Coke is essentially coal with the “junk” removed. The water, sulfur content, tar, and other components of the coal are driven off to leave a high carbon content product. This product is generally used in the reduction of iron ore into iron in direct reduction processes. This process requires temperatures around 1000-1100°C and requires a heat input, but the process relies on the very dirty coal product. This processes using coke will hopefully become obsolete rendering the production of coke useless. The second product is the production of quicklime from calcium carbonate. This product is important component of cement and as a result has a high demand due to the use of concrete. Quicklime is formed through the release of carbon dioxide from calcium carbonate containing limestone.

$$CaCO_3 \rightarrow CO_2 + CaO \quad (2.2)$$

Studies by meier et al. have shown a successful production of lime in a solar thermal reactor.[5] This analysis produced lime with higher purity than typical industrial lime using only solar input. With efficiencies near 35%, the process was able to reduce the CO_2 emissions of the process by 20-40% compared with industry. The one drawback of the process is the cost. The cost was estimated at about 2-3 times the cost of conventional lime.

Several metals were also considered as the end product of a solar chemical cycle. These metals included metals such as: Zinc, Magnesium, Tin, Copper, Iron and Nickel. Although there are inherent differences between the common ores and properties of each metal, the methods of production for each metal tend to be similar. These methods included: reduction using a reducing agent such as hydrogen, electrolysis, and on rare occasion, direct decomposition. The direct decomposition temperatures of these metals all exceeded 1500°C making this process infeasible for coupling with our CSHSS currently under development. However, similar to the case with tungsten, the limiting factor is not the capabilities of the concentrated solar power, but is instead the materials capabilities of the solar receiver and other design components. The electrolytic production method of these metals is another possible production method which requires electricity to produce. The CSHSS could be used with an electricity generating cycle to produce electricity of the electrolytic production of metals using high temperature heat to reduce electric demand similar to the proposed production of magnesium by Sheline et. al.[6] Although this would be a feasible design, the implementation would require electrolytic components, rankine cycle components and other machinery that would complicate the system. Since the CSHSS design is reaching pilot scale size, an easily implemented immediate solution is desired. This leaves the final method of creating metals with a reducing agent. Iron, for example, uses a direct reduction process that uses coal as the fuel. This process reacts Iron ore (Fe_2O_3) with carbon monoxide to form Iron. Although the process is simple and robust, this process produces large amounts of slag waste, produces harmful gas products, and suffers maintenance issues caused by coking. The use of hydrogen with solar heat would be a sustainable, lower maintenance alternative for producing metals.

2.1 Hydrogen Production

The production of metals using hydrogen reduction would require the production of hydrogen from another source. Two potential sources were examined. One source is through the use of methane gas and steam. By reforming methane using high temperature heat, a high hydrogen concentration synthesis gas can be created. The second source is through the hydro-cracking of ethane into ethylene. This process is done in the chemical industry to produce ethylene as a feed stock for polymers. The byproduct of the reaction is hydrogen which can be separated and used for the metal reduction process.

The first source is through the well-developed steam methane reformation process. This process uses methane gas with high temperature steam to produce high hydrogen concentration synthesis gas. The reformation is a two-step process. First, the methane is reacted with steam in the Steam-Methane Reforming (SMR) Equation to produce hydrogen and carbon dioxide shown below. Then, the resulting gas is further reformed with more steam in the Water Gas Shift (WGS) reaction to produce even more hydrogen.

Steam-Methane Reforming Equation: $CH_4 + H_2O \rightarrow CO + 3H_2$ (2.3)

Water Gas Shift Equation: $CO + H_2O \rightarrow CO_2 + H_2$ (2.4)

The SMR reaction is considered one of the better methods for reforming methane into hydrogen due to the high hydrogen yields, but it has the drawback of requiring a large amount of heat to produce.[7] This is perfect for a CSHSS as the solar energy can act as the heat supply instead of burning the very exergetic methane gas for heat. In addition, the optimal SMR reaction requires reaction temperatures around 750°C which is near the 1000°C capabilities of the CSHSS system. The WGS reaction on the other hand is slightly exothermic and does not require heat. Based on the heat requirement of creating steam from water and the enthalpy of reaction of the SMR equation, a minimum of three-eighths a mole of methane needs to be burned to provide heat to the system per mole of methane reformed, assuming no losses. This fuel savings could allow the production of 40% more hydrogen for the same amount of methane or 40% more metal, if used in conjunction with a metal ore reduction process.

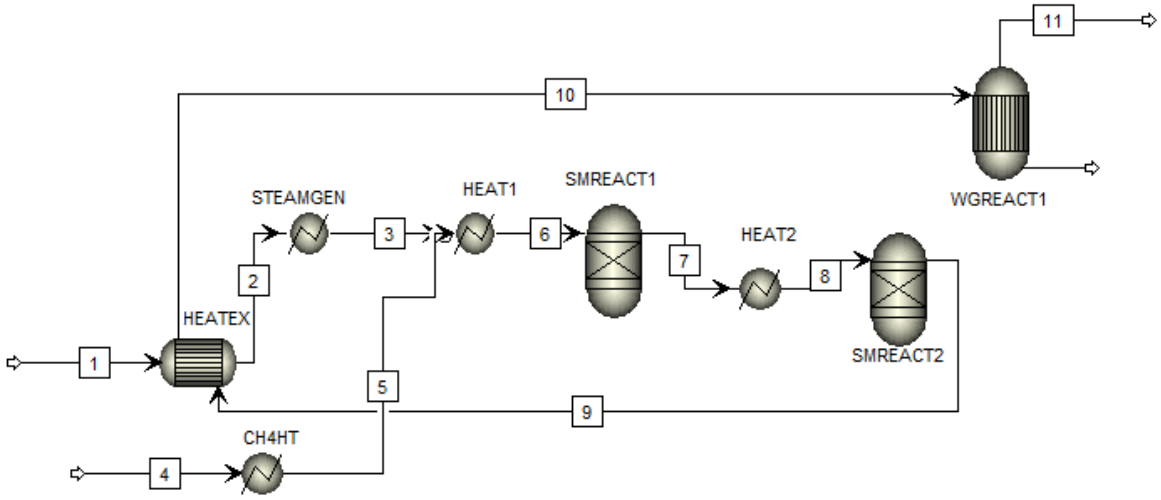

Figure 2: ASPEN PLUS thermodynamic model of steam methane reformation process

A thermodynamic ASPEN PLUS model was created to develop a Q vs T diagram of the heat exchange between the particulate storage medium of our CSHSS and all of the components in the chemical reformation process. The ASPEN PLUS diagram is shown in Figure 2. In this figure, there are 3 reactors: a low temperature SMR reactor, a high temperature SMR reactor, and the WGS reactor. The various heaters are for generating the steam and heating the reactants to the required reaction temperature. At stream 1, water is input at ambient condition. Heat recovered from the high temperature methane reactor is used to heat the water to a saturated liquid. The steam generator heats the water at constant temperature to a saturated liquid. Preheated methane from stream 5 is mixed with the steam before a heater heats the mixture to the temperature of the low temperature reactor. The mixture is reacted in the low temperature reactor to the thermodynamic equilibrium

of the SMR reaction. The mixture is then heated to the high temperature reaction temperature and is again reacted to thermodynamic equilibrium in the higher temperature SMR reactor. The mixture is then reacted a final time in the WGS reactor before the final products are produced at stream 11. The resulting products are shown in Table 1. The table shows that the methane was reacted into a high concentration hydrogen stream with over 75% of the final product being hydrogen. The products are based on a 1 kmol/sec input of methane at stream 4. Other products included carbon dioxide, steam, methane and some carbon monoxide. The WGS and SMR reactors could be further optimized based on desired outputs. For example, the excess steam could be increased to reduce leftover methane, a lower temperature WGS reactor could be added to reduce carbon dioxide, etc.

Table 1: Steam methane reformation products

Methane	88.9	**kmol/hr**
Water	756.6	**kmol/hr**
Carbon Monoxide	578.8	**kmol/hr**
Hydrogen	**13465.6**	**kmol/hr**
Carbon Dioxide	2932.3	**kmol/hr**
% H2 Yield	75.6	**%**

The results from the thermodynamic model were used to produce a Heat Rate vs Temperature diagram. The heat rate diagram simulates the heat exchange between the particulate medium of the CSHSS and the various components of the chemical reformation process. The heat rate diagram is dependent on the maximum temperature of the sand, the change in temperature of the sand, and the setup of the chemical reformation diagram shown below. The temperatures for the sand were chosen to fit well with the heat rates of the chemical reformation process with a delta temperature of approach of around 100°C. The diagram was iterated several times to create a heat rate diagram with the minimum exergy destruction. The minimum exergy destruction is produced when the difference between the integral of Temperature with respect to the Heat Rate of the sand side and chemical process side is minimized. Minimizing this exergy destruction is the reason for separating the SMR reaction into a low temperature and high temperature reactor. This allows some of the heat input to be input at a lower temperature, better fitting to the straight sand line. The final Temperature vs. Heat Rate diagram uses the heat rates from the various components in Figure 2 to produce Figure 3. The chart shows from left to right: the preheating of the methane in CH4HT, the generation of steam in STEAMGEN, the heating of the mixed methane and steam to the low temperature SMR reactor temperature in HEAT1, the reaction of low temperature reactor in SMREACT1, the heating of the mixture to the high temperature SMR reactor temperature in HEAT2, and finally the reaction of the mixture of the high temperature SMR reactor in SMREACT2. The WGS reactor is not shown in the chart as this reaction is slightly exothermic and does not require any heat input. Although this heat could be recovered, it is doubtful that it would be economical to recover the small amount of heat produced by the WGS reactor.

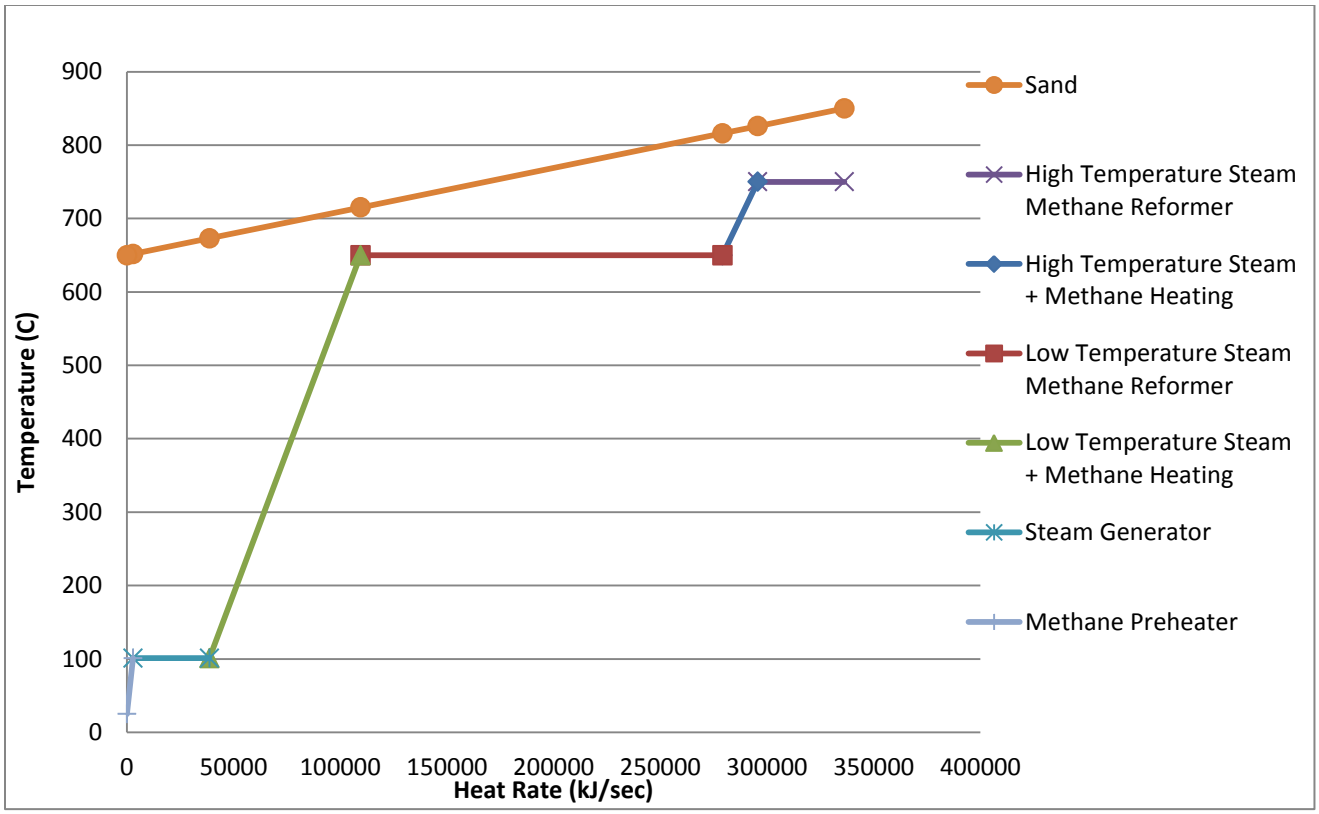

Figure 3: Steam-Methane Reformation Temperature vs. Heat Rate diagram

The second source is the ethane hydro-cracking process. This process promises to produce both the product of ethylene and the hydrogen necessary for metal reduction. In addition, the ethane hydro-cracking process requires additional heat that can be supplied by the CSHSS. Although more complex, by coupling a ethane hydrocracking process to a metal reduction process such as the reduction of iron ore, heat from the CSHSS could be used to produce two products, iron and ethylene, simultaneously. The Iron-Ethylene process was selected for further study, but there is also ongoing research on the steam methane reformation process for the production of hydrogen.

Although the methane hydrogen process is also being investigated, we decided to pursue the ethylene process as the source of hydrogen for the iron reduction process. There are several reasons for this decision. First, the methane reformation process requires the consumption of methane which will bring added cost to the system. This process also produces some carbon dioxide pollution. In addition, the ethylene process produces a second product that will be valuable to the overall production cost. The drawback of this system includes the added complexity and the capital costs associated with the much larger chemical process. With a much larger capital cost and more complexity adding risk to the feasibility of the cycle, it may be difficult to get investment. Iron was selected as the metal to be produced, but almost any metal could be produced. Iron was selected because a large volume of this metal is produced every year. Because of the large volume, we believe this metal would be in higher demand.

3. Process Overview

An Iron hydrogen reduction process was coupled with the ethylene production process as the source of hydrogen to create a combined Iron-Ethylene Solar production process. The proposed Iron-Ethylene process is characterized by the following reactions:

$$C_2H_6 \rightarrow C_2H_4 + H_2 \quad (3.1)$$

$$Fe_2O_3 + 3H_2 \rightarrow 3H_2O + 2Fe \quad (3.2)$$

The proposed Iron-Ethylene process would use heat from a 50 MW CSHSS to separate ethylene from ethane as shown in Equation 3.1 and, by using the hydrogen formed from the ethane cracking, to reduce iron ore into iron as shown in Equation 3.2. Both of these reactions require significant heat input that would be supplied by the CSHSS. Normally this required level of energy input is generated by the burning of fossil fuels which have a cost associated with them and are subject to significant price fluctuations. Replacing the fossil fuel energy input with solar energy has the potential to: eliminate the required capital cost and risk associated with fuels, reduce capital cost, and reduce pollution by being a completely clean and sustainable technology while producing high value iron and ethylene products (with the additional byproduct of water).

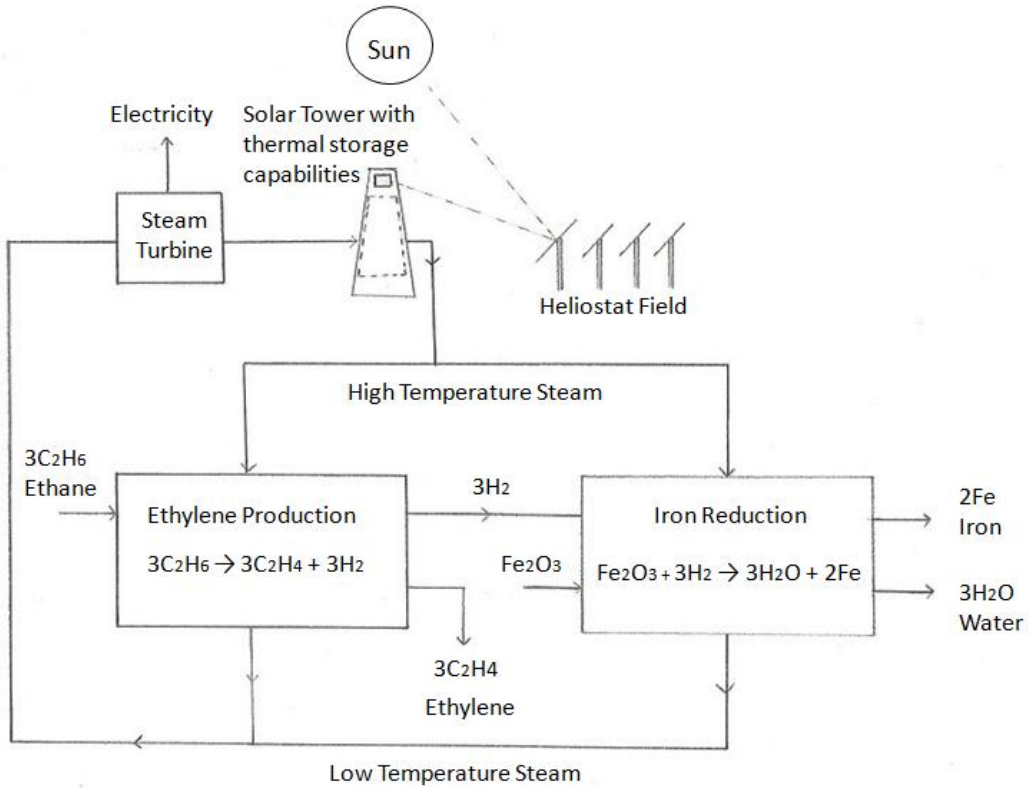

Figure 4: Cycle overview

Figure 4 shows a complete overview of the process. The process begins by utilizing a CSHSS with the ability to store thermal energy. The stored thermal energy will allow for the regulation of the thermal energy input as well as the possibility of producing products beyond the hours of normal solar input. The stored thermal energy can then be delivered to the two endothermic reactions via one of two proposed methods. The thermal energy can be used to generate steam that will be used in the chemical processes, or the thermal energy can be directly exchanged with each of the chemical components. The steam method would make the entire process less complicated and allow for the transportation of the thermal energy to a nearby plant, but would be much less efficient. The direct heat exchange would require much more research and development and would require the chemical process to be integrated into the tower, but would be much more efficient. Using this thermal energy, the chemical process can take place. First in the ethylene production process, ethane is split into ethylene and hydrogen. Once the products are separated, the hydrogen is then input into the iron production process. Iron and water are produced by reducing iron ore with the hydrogen. Finally, heat recovery could allow for the lower temperature thermal heat to be used in a bottoming cycle such as a Rankine cycle. This could allow for on-site production of the entire plant's electricity needs, eliminating the need for electrical transmission to the site. This would be especially advantageous if the CSHSS is in a remote area such as a desert.

A full design stage analysis of the cycle was performed. Included in this document is: a feasibility study of the CSHSS including the economic and energy payback for a 10 MW_{th} and 50 MW_{th} CSHSS[8], and a full thermodynamic analysis of the chemical cycle. The full thermodynamic analysis includes an ASPEN PLUS model the cycle, the projected production rates of products for a 50 MW_{th}, a Energy (first law), Entropy (second law) and Exergy (combined law) analysis of the cycle, and finally a heat rate vs temperature diagram of the heat exchange between the CSHSS and the chemical components. In addition, this Q vs T diagram also includes the exergy destruction of this heat exchange, and a comparison to the exergy destroyed by a typical Rankine cycle.

4. Solar Power Tower Energy Quantification/Feasibility Study

The above described cycle has two essential components: the heat supply system supplied by concentrated heat, and the chemical process that consumes the heat to produce a chemical product. Since the CSHSS is essentially supplying high temperature heat to these processes, it has the potential to be replaced with heat produced by less clean burning fossil fuel substitutes or potentially other renewable technologies. Because of this, a feasibility study for the use of a CSHSS was performed to compare the projected economic costs and output of various sized (10 and 50 MW_{th}) CSHSS to the cost of fuels burned. This allowed a calculation of the economic payback. In addition, an energy payback analysis compared the energy payback time of the CSHSS to various fossil and renewable energy supplies. The 10 MW_{th} CSHSS data was based on an actual design for a pilot plant sized CSHSS being developed at Georgia Tech. The 50 MW_{th} CSHSS data was based on results obtained by using the National Renewable Energy Laboratory (NREL)'s Solar Advisor Module (SAM).

4.1 Energy and Economic Data Inputs – Secondary Research

The calculation of the energy payback ratio, energy payback period, and economic payback period required several estimates and data inputs. First, a preliminary design of the tower and heliostat field to support further calculations was created. The proprietary heliostat field layout and heliostat design[9] were provided by Solar Tower Systems, a possibly subcontractor for heliostat systems. The central tower design[10] was created by scaling and modifying the design of an already constructed 300 kW pilot plant. Second, an estimate of the annual energy collected was found based on: the expected incident solar radiation, ambient conditions, and the expected optical and thermal performance of the heliostats and the receiver. This included the hourly incident solar radiation provided by the National Renewable Energy Laboratory's (NREL) Solar Advisor Module.[11] Third, the amount of each raw material needed in the construction of CSHSS was estimated. This included materials such as mirror glass, steel, and other materials needed in the heliostats, steel and concrete in the structure of the tower and foundation of the heliostats, and other materials for the remaining subsystems. The amount of each raw material for the heliostat system was provided by Solar Tower Systems, while the amount of each material for the central tower was quantified using the model of the preliminary tower design. Fourth, energy embodiment data was acquired for the primary energy consumed in producing, transporting, and assembling each material into a finished system. Table 2 shows the data used to determine the energy cost of constructing a 10 MW thermal CSHSS. The energy costs per unit volume were provided from an article by Reddy and Jagadish (2002) published in the journal *Energy and Buildings.*[12] These published energy costs included the full life cycle energy required to produce each material. For example, the energy cost of steel includes all of the energy required to mine the iron ore, transport it to the steel factory, and refine the ore into steel. Finally, cost data was acquired for the materials, labor, construction overhead and infrastructure, profits, and other fees for manufacture and construction of the various components and subsystems. The economic data was taken from the industrial-standard online construction cost data base maintained and published by the R. S. Means Corporation (2008).[13]

Table 2: Material Production Energy and Economic Data

Material	Production Energy (MJ/m^3) (Ref [12])	Transportation Energy ($MJ/100km*m^3$) (Ref [12])	Total Energy Cost	Total Construction Cost ($\$/m^3$) (Ref [13])
Burnt Clay Brick	2141	200	2341 MJ/m^3	2185
Glass	61920	200 (4)	62120 MJ/m^3	22036
Reinforced Concrete	3640	182.4	3823 MJ/m^3	732.8
Concrete	1970	179.3	2150 MJ/m^3	(3)
Sand	0.0	175	175 MJ/m^3	10.0
Crushed Aggregate	20.5	175	195.5 MJ/m^3	(3)
Portland Cement	11759	201	11960 MJ/m^3	(3)
Steel	336000	800	336800 MJ/m^3	28572
Aerated Concrete	1970 (1)	179.3 (1)	2150 MJ/m^3 (1)	385.1
Reinforced Concrete Slab Floor	(2)	(2)	730 MJ/m^2	732.8

Construction Energy Cost	10000	MJ/m^2	Ref [19]

(1) Assumed to be the same as for standard concrete

(2) Only the Total Energy Consumption data is required

(3) The Total Construction Cost of the concrete, sand, crushed aggregate, and Portland cement are all combined in the reinforced concrete cost. Sand is also used as the thermal energy storage medium.

(4) The energy for transportation for glass was assumed to be the same as that for burnt clay brick.

The feasibility of the CSHSS is based on two analyses: the economic payback and the energy payback. The economic payback period and the rate of return of the tower is an important metric to determine the market feasibility and financial benefits of the CSHSS while the energy payback gives insight into the net amount

of thermal energy collected by the energy conversion device. First, this paper explores the energy payback of a 10 MWth CSHSS where MWth represents thermal heat produced, not to be confused with the electrical work produced. The energy payback is calculated as thermal heat because it will be used to produce heat for a chemical process and its primary purpose will not be to produce electricity. The energy payback includes the calculation of the materials and construction energy cost followed by an estimate of the parasitic losses of the CSHSS caused by the lift elevators associated with the thermal storage medium. This CSHSS energy payback is compared to the energy payback of other energy conversion devices. Second, the economic payback is estimated for both a 10 MWth and 50 MWth CSHSS. This economic analysis finds the simple payback period and Rate of Return of the CSHSS when compared to the fuel savings of a traditional fossil fuel system.

4.2 Energy Collected by CSHSS

The total thermal energy collected by the CSHSS was estimated using the "hourly thermal energy supplied by the solar field" produced by the Solar Advisor Module (SAM). This data was based on hourly incident sunlight weather data (in kWh) for Riyadh, Saudi Arabia over one complete year. It was modified to account for reflection losses, re-radiation losses, and convection losses. Effects caused by the efficiency of the heliostat field (including incident cosine efficiency, blockage efficiency, etc) were calculated using SAM's built in Delsol program. Using the data from SAM, a reflection coefficient of 0.9 was used, an emissivity of 0.9 and operation temperature of 1273 K (1000°C) was assumed for re-radiation and the hourly ambient temperature was used for convection losses with a 28.5 W/(m^2*K) convection coefficient.[14] After all the losses were applied to the incident radiation according to Equation 4.1, the hourly energy collected was summed for the entire year to find the total energy collected for one year. The results indicate that $6.2*10^7$ and $3.5*10^8$ MJ of thermal energy would be collected for the 10 MW_{th} and 50 MW_{th} CSHSSs respectively.

$$E_{Collected} = \sum_{i=1}^{8760} (E_{Incident,i} - E_{Losses,i}) \quad (4.1)$$

In addition to the losses calculated here, there may also be losses caused by the transient nature of the thermal storage. If the plant is required to warm up and shut down every day, a certain amount of the energy collected from the morning hours of the day will be required to bring the thermal mass up to the required temperature before any reactions occur. This means in the energy collected in the morning hours will be unusable for the high temperature application. However, the transient on the cool down also would allow for heat that can be used for some purpose. Another major factor is the amount of thermal storage included in the thermal tower. Ideally, the tower would have enough storage to operate 24 hours a day, and thus would not have any transient losses. Due to the unknown thermal storage capability and warm up characteristics, no transient losses were included at this point in the analysis.

4.3 Energy Payback Analysis

A full cycle energy analysis seeks to quantify the energy consumed and produced by the system at every stage of development. This means the energy required to mine the materials, transport the materials, construct

the tower, etc. are all included in the energy consumption. For the CSHSS the energy consumed includes the energy required in: the production of the raw materials (mostly steel, concrete and glass), the transportation of the materials to the site, the construction of the CSHSS, and the operation of the CSHSS. The energy required in the production of the raw materials includes all of the energy in mining the raw materials, transporting it to the refining factory and producing the product.

Since CSHSS technology is fairly new, no estimate of the deconstruction and decommission of the tower was made, but this has been shown to be small in comparison to other components of the life cycle analysis for other energy conversion devices.[15] The energy produced by the CSHSS was expressed as thermal energy collected by the solar receiver over a full year in Riyadh, Saudia Arabia (a potential location of this system). We propose using this thermal energy for the production of ethylene and iron, but it could also be used for other applications such as electricity generation. The energy payback period was expressed as the time (in years) to produce enough thermal energy to offset the thermal energy consumed in constructing and operating the CSHSS. Dividing the lifetime of the tower (30 years) by this energy payback period allows the energy payback to be expressed as an "Energy Payback Ratio." This energy payback ratio is used by other authors and could be useful in comparing the energy payback to previously published works on coal, nuclear, photovoltaic and other energy conversion devices [16,17,18].

The energy payback was first calculated with the thermal energy required to construct the tower. The energy required for the material and construction portions of the CSHSS are calculated using the metrics in Table 2. First, to calculate the energy required for the materials, the amount of each material required was calculated. With the amount of each material required, the production energy cost of each material type was found by multiplying the amount of the material required by the cost metric. The transportation energy cost (the energy cost to transport the materials to the construction site) was assumed to be for a distance of 100 km. The last component of the energy cost is the construction energy cost. This was found by using the energy consumption costs for the construction of similar large office buildings.[19] Summing the transportation energy cost, the production energy cost and the construction energy cost produces the total energy consumption. The transportation energy cost was a very small contribution to the overall energy cost. Also note that the energy value for reinforced concrete was based on a weighted average of sand, aggregate, cement, and steel. The cement, sand and aggregate were mixed at ratios of 1:2:3 by volume to make concrete and the reinforced concrete was a mixture of steel and concrete with steel composing .005 of the total reinforced concrete cross-section.

The energy cost of the tower is shown in Table 3. The estimate for the material requirements was calculated in SolidWorks using the internally developed design. The volume of each component was determined using SolidWorks 2012's mass properties function.[20] The tower consisted mostly of structural Reinforced concrete, insulating Aerated concrete, insulating firebrick, steel from the machinery and sand as a thermal storage medium. The heat exchanger value was applied based on a nominally 1000 pound heat exchanger for a 300 kW_{th} system scaled to a 10 MW_{th} system. Multiplying the energy metrics by the volume of each material allowed for the calculation of the material cost and similarly, the weight of each material was used to find the transportation cost. The construction cost of the tower was found using the tower's maximum floor area of 250 m^2 and by using the energy costs from a study of the construction of large office buildings. The construction cost

accounted for approximately 10-11% of the total energy cost. The resulting total energy cost for the tower subsystem was estimated to be 25 TJ thermal.

Table 3: 10 MW_{th} Tower Energy and Economic Costs

Component	Material	Volume (m^3) (ref [10])	Floor area (m^2)	Energy Metric	Cost Metric ($/$m^3$)	Cost ($)
Floor 1	RC concrete	62.4	249.6	730 (MJ/m^2)	732.8	$4.57x10^4$
Floor 2	RC concrete	60.6	242.4	730 (MJ/m^2)	732.8	$4.44x10^4$
Floor 3	RC concrete	48	192	730 (MJ/m^2)	732.8	$3.52x10^4$
CSP Round Tower	RC concrete	2263	-	3823 (MJ/m^3)	732.8	$1.66x10^6$
Foundation	RC concrete	625	-	3823 (MJ/m^3)	732.8	$4.58x10^5$
Thermo bin	RC concrete	1100	-	3823 (MJ/m^3)	732.8	$8.06x10^5$
Insulation	Aerated Concrete	1695	-	2149 (MJ/m^3)	385.1	$6.53x10^5$
Thermo bin	Firebrick	41	-	2341 (MJ/m^3)	2184.8	$8.96x10^4$
Heat exchanger insulation	Firebrick	3.8	-	2341 (MJ/m^3)	2184.8	$8.30x10^3$
Olds elevators	Steel	6.3	-	336800 (MJ/m^3)	28571	$1.80x10^5$
Storage medium	Sand	442	-	175 (MJ/m^3)	10	$4.42x10^3$
Heat exchanger	Steel	1.875	-	336800 (MJ/m^3)	28571	$6.32x10^5$

Tower Construction Energy Fraction	10.1	%
Construction Energy Requirement	2496000	MJ
Total Tower Energy Requirement	2.48E+07	MJ
Total Tower Cost	**$4,040,000**	
Estimated Receiver Cost	**$1,000,000**	

The final energy cost of the heliostat field is shown in Table 4. The energy cost of the heliostat system was found using the process described above to find the material cost, transportation cost and construction cost. Based on the Solar Tower System's estimates, each heliostat requires 200 kg of steel, 800 kg of concrete, and 15 kg of glass. The heliostat field required for a 10 MW_{th} design has 1736 heliostats. This estimate had close agreement to the 1715 heliostats predicted by a SAM model for the same sized CSHSS. The construction cost was calculated as a percentage of the total material and transportation cost. This percentage was found by dividing the construction energy tower cost by the total tower energy cost. The total cost for the heliostat field subsystem was estimated to be 18 TJ thermal.

Table 4: 10MW_{th} Heliostat Field Energy and Economic Costs

Number of Heliostats	1736 (ref [9])	# Heliostat
Total Heliostat Mirror Area	12733 (ref [9])	m^2

Material	**Material Weight (m^3/Heliostat)**	**Energy Metric (MJ/m^3)**	**Cost Metric ($/$m^3$)**
Glass	0.00625	61920	22036
Steel	0.025	336800	28572
Concrete	0.338	3823	732.8

Total Energy Required per Heliostat	9450	MJ/Heliostat
Total Cost per Heliostat	1100	$/Heliostat
Construction Energy Requirement	1.65×10^6	MJ
Total Heliostat Energy Required	1.81×10^7	MJ
Total Heliostat Cost	**$1,904,000**	

The final summed results for the energy payback is shown in Table 5. The total energy embodiment of the CSHSS was calculated by summing the heliostat and tower energy costs. The receiver energy cost was not included because of the experimental nature of current designs. The Energy Payback Period (in years) was determined by dividing the total energy cost of the CSHSS by the energy collected in one year. The nominally 10 MW_{th} system has a total energy cost of 43 million MJ_{th} with an annual energy collection of 62 million MJ_{th} per year giving an energy payback period of less than one year, or about 250 days without contributions from the parasitic losses.

Table 5: Results of Energy and Economic Analyses

	10 MW (Materials Estimate)	50 MW (SAM Estimate)	Units
Total Energy Embodiment	4.29E+07	-	MJ
Energy Collected (1 year)	6.21E+07	3.50E+08	MJ/year
Energy Pay Back Period (no parasitic losses)	0.69	-	years
	252	-	days
Total Economic Cost	$6,950,000	$25,520,000	
Energy Value (Methane)	4.74	4.74	$/GJ
Energy Value (Petroleum)	15.3	15.3	$/GJ
Collected Energy Value (Methane)	$368,000	$1,660,000	$/year
Collected Energy Value (Petroleum)	$1,190,000	$5,370,000	$/year
Simple Economic Payback Period (Methane)	19.03	15.4	Years
Simple Economic Payback Period (Petroleum)	5.88	4.8	Years
Rate of Return (Methane)	4.3	5.8	%
Rate of Return (Petroleum)	17.0	21.0	%

* For the Rate of Return, the parasitic loss of the combustion process and solar process are assumed to be equal

* Low energy value corresponds to price of around 5 $/MMbtu Natural Gas burned at 100% combustion efficiency

* High energy value corresponds to price of around 90 $/bbl crude oil (5.8 million BTU/bbl) burned at 100% combustion efficiency

4.4 Parasitic Loss of Elevators

Next, the estimate of the parasitic losses was added to the energy analysis. There are two important particle handling elevators in the proposed CSHSS system with thermal storage: the elevator that lifts lower temperature particulate from the discharge of the storage bin near the base of the tower up to the receiver and shorter elevators that recirculate particulate being heated in the receiver. Currently, the preferred lift elevator (LE) is a continuous chain bucket elevator designed to handle particulate around 600°C to 700°C. Although these temperatures are high, they are within the range of conventional materials. Conversations with practitioners experienced in handling granular materials indicate suitable bucket elevators are available.[21] The recirculation elevator (RE) must operate at higher temperature in the limited space in proximity to the receiver. The preferred design is the OLDS elevator (see US Patent 7,314,131) which is a simple, compact, robust, and wear-resistant

design. The OLDS elevator operates using the same principles of the classic Archimedes screw. Unlike the Archimedes screw, the central helical screw is fixed while the outer drum rotates entraining the particulate up the helix.

The parasitic power consumed by these two elevators is another contribution to the energy cost of the tower. The lift elevator is shown schematically in Figure 5. This figure also shows the height the recirculation elevator would lift sand (the height of the Solar Receiver). During collection, the LE will typically lift twice the mass flow rate necessary to energize the power plant. Half would be used for immediate generation and half would be stored for later generation during the night. The RE will only operate to recycle partially heated particulate back through the solar receiver as necessary. This would be necessary if the sand was not heated to the required temperature after the first pass. Thus, this elevator only needs to lift particulate from the bottom to the top of the receiver. The number of recirculation passes necessary will depend on the overall increase in particulate temperature (ΔT) required and the temperature rise achieved in each pass.

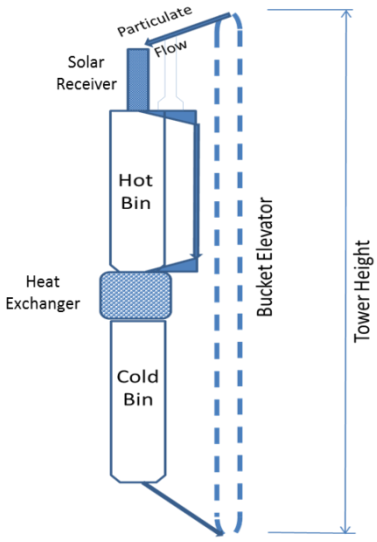

Figure 5: Schematic of Particulate Flow Showing Lift Elevator

The parasitic losses from the two elevator systems are best presented as fractions of the electric power that could be produced from the thermal energy collected. This parasitic fraction depends primarily on the required ΔT of the particulate and the height of the tower. It is defined as:

$$F_{\mathrm{PAR}} = \dot{W}_{\mathrm{PL}} / \dot{E}_{\mathrm{COLL}} \tag{4.2}$$

The rate of electric power produced from the thermal energy collection is:

$$\dot{E}_{\mathrm{COLL}} = \left(\dot{m}\, C_P\, \Delta T\right) \eta_{\mathrm{CONV}} \tag{4.3}$$

where $\dot{m}$ is the mass flow rate through the power cycle heat exchanger, C_p is the average specific heat of particulate such as sand, taken to be quartz, with specific heat around 1050 J/kg-K at elevated temperature[22], ΔT is the total increase in particulate temperature across the solar receiver in one pass, and η_{CONV} is the heat to work conversion efficiency of the thermal power into electrical work. The system assumes a conventional conversion efficiency of 40% corresponding to the typical efficiency attainable in coal power plants.[23] The corresponding parasitic power loss is:

$$\dot{W}_{PL} = \left(\dot{m}\, g\ H_L\right) R_{OP} / \eta_{EL} \tag{4.4}$$

where $\dot{m}$ is the flow rate, g is gravitational acceleration, H_L is the tower height, R_{OP} is an operational ratio (defined differently below for the LE and the RE), and η_{EL} is the energy efficiency of the elevator.

For the LE, a bucket elevator, an efficiency of 80.5% was used.[24] For a typical CSHSS system some thermal energy will be converted to power during solar energy collection and some will be stored. The operation ration accounts for the storage of thermal energy. For a two bin design, twice the particulate required to energize the power cycle will be lifted to the receiver during solar collection with half then immediately directed to the heat exchanger, and half directed to the hot bin. After the collection of solar energy ends for the day, the stored particulate flows by gravity alone through the heat exchanger. This means the average flow through the receiver is the same as the average flow through the heat exchanger over an entire day, resulting in an operation ratio of 1:1. The amount of energy collected was calculated for a ΔT across the receiver of 250-350 K and the parasitic loss was calculated for a H_L of 100-160 m. This height range was adopted based on a plant capacity to height comparison.[25] It roughly corresponds to a plant capacity of 1-50 MW. As seen in the accompanying figure (Figure 6), the parasitic loss for the LE ranges from a high of 1.9% (at the lowest ΔT of 250K and highest H_L of 160m) to a low of 0.8% (at the highest ΔT of 350K and lowest H_L of 100m). While a considerable amount of power is required to drive the LE, the high ΔT anticipated in the receiver system achieves a large energy collection per unit mass of particulate lifted resulting in a low parasitic energy fraction.

The calculation for the recirculation elevator (RE) power consumption is similar to the full tower lift calculation shown above, but for the RE, the parasitic loss is based on a number of 10m (the height of the receiver) recirculation passes. The height, H_L = 10m while the R_{OP} accounts for the number of recirculation passes in the receiver, and the η_{EL} is changed to reflect the efficiency of the OLDS elevator. Based on preliminary laboratory tests this efficiency is around 25%.[26] Measurements of the elevator efficiency for a small scale model for various models of the OLDs elevator showed an elevator efficiency of at most 17%. This number would of course improve for larger scale models of the elevator, but it is an indication of the improvements that need to be made. Since the OLDS elevator relies on friction to lift the particulate, it is inherently less efficient than a bucket elevator. Although the OLDS elevator has a relatively lower efficiency, it is a much more compact, rugged, and temperature-resistant system making it advantageous for short lifts in the high temperature and confined receiver space. With a R_{OP} ranging from 1 to 5 the parasitic fraction for the RE ranges from 1.9% (at the lowest ΔT of 250K and highest R_{OP} of 5) to a low of 0.3% (at the highest ΔT of 350K and lowest R_{OP} of 1). Results for both the LE and RE are shown in Figure 6 and 7.

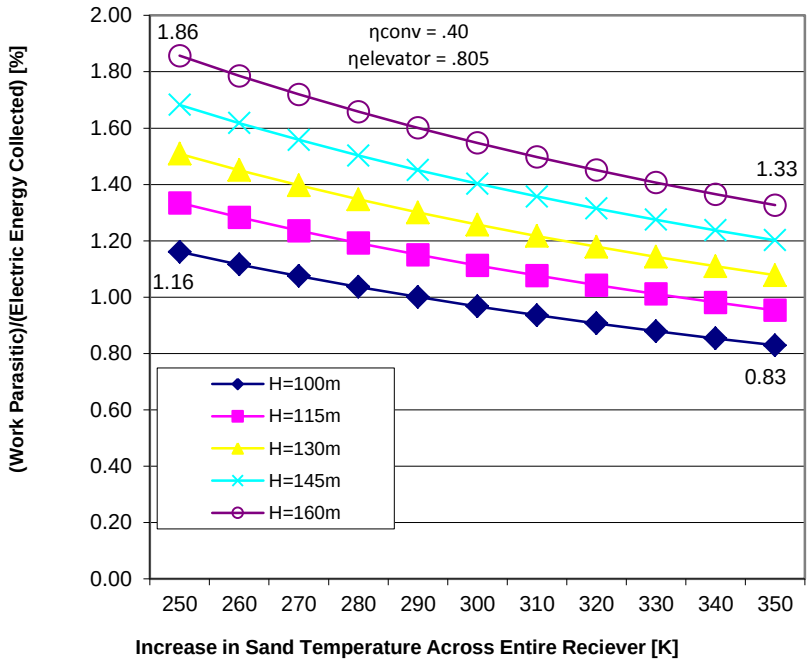

Figure 6: Lift Elevator Parasitic Loss Fraction

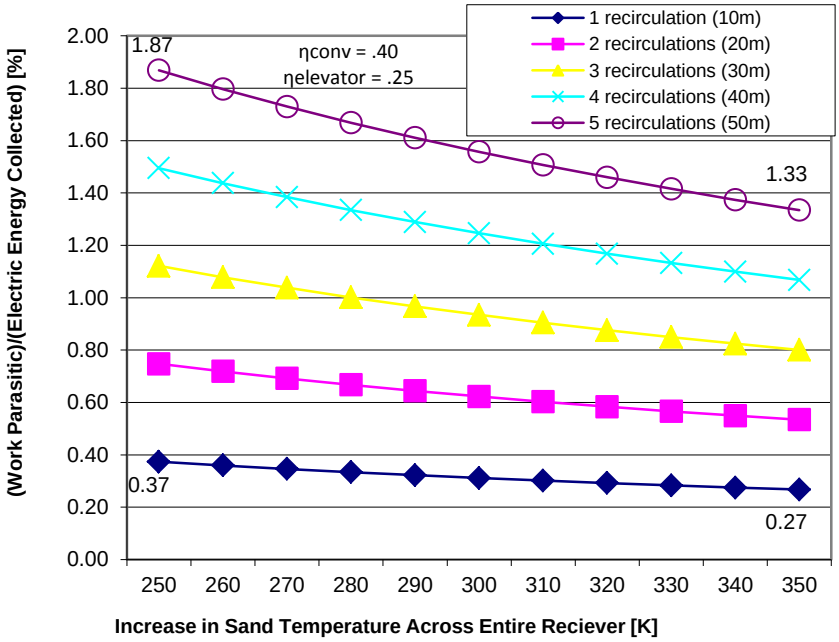

Figure 7: Recirculation Elevator Parasitic Loss Fraction

To find the total parasitic loss, the percent loss from the full tower lift can be added to the percent loss from the recirculation. This overall parasitic fraction should be in the range of 1.1% (100m tower, ΔT of 350K, no recirculation required) to 3.7% (160m tower, ΔT of 250K, 5 recirculation passes required). This parasitic loss fraction is small primarily because of the large temperature rise in the particulate. This overall loss is much smaller than the acceptable parasitic power consumption (for cooling fans, pulverizers, pumps, etc.) in conventional power plants such as pulverized coal plants and will not have an unacceptable effect on net output, plant net efficiency, or the Levelized Cost of Energy.[27] However, this parasitic loss fraction only includes the largest anticipated component of the parasitic loss and additions of other losses such as the heliostat motion, internal monitoring equipment, pumps etc. will increase the overall parasitic loss.

4.5 Parasitic Loss of Heliostat and Other Auxiliary Losses

Other important parasitic losses included the movement of the heliostat field, and other auxiliary systems required in the operation of the power tower. The heliostat field parasitic loss includes all of the power required for the heliostats to track the sun. Due to the large number of heliostats, this may seem like a very large number, but the heliostats only rotate a very small amount per day (about a half revolution). A report by Sandia National Laboratories found the parasitic loss of two large scale heliostats to be 292 Wh and 385 Wh per 10 hour day for a 148 m^2 and 200 m^2 heliostat respectively.[28] This data was used to find the parasitic loss fraction of the heliostat field similar to the elevators above. The parasitic loss of the heliostat field is shown below:

$$F_{par,helio} = \frac{(P_{consume} / A_{Helio}) A_{Helio,tot}}{\dot{E}_{\text{collected}} \eta_{th}} \tag{4.5}$$

In Equation 4.5 above, $P_{consume}$ and A_{Helio} represent the power consumed and area of the heliostat in the test reported by Sandia Laboratories. $A_{Helio,tot}$ represents the total heliostat area in the 10 MW_{th} heliostat field. Finally, the $E_{collected}$ and η_{th} are the energy collected and practical thermal efficiency (40%) given above. Since the scale of the heliostat will also affect the power consumption per m^2, the parasitic loss was also calculated by extrapolating the power consumption per m^2 to take into account the different size of heliostat. The difference between to parasitic loss for the two cases was less than 10% and the highest value was chosen to be conservative. The overall parasitic loss for the heliostat field was 0.14%.

The next parasitic loss that needs to be accounted for is an estimate of the operation of any controls and equipment the plant may require. Since the designs for our tower do not yet include these components, they will be estimate based on data from a typical coal power plant. Table 6 below shows data from Sargent & Lundy LLC.[29] The parasitic loss percentages represent three main categories: parasitic losses for the power cycle including fan power, pumps etc. (first 9 components), fuel handling and environmental parasitic losses shown in bold, and miscellaneous parasitic losses. Almost all of these parasitic losses no longer are required in the CSHSS.

The CSHSS no longer requires fans for the combustion chamber, fuel handling, or any environmental air scrubbing equipment. The remaining components for the pumps would only be utilized in the power cycle not in the CSHSS. However, the CSHSS is being pair with a chemical cycle, and could also be used to generate electricity. Because of this, the parasitic loss was calculated with a low and high estimate. The low estimate represents parasitic losses for only the CSHSS (miscellaneous loss only) while the high estimate includes all of the losses from Table 6 except the environmental air scrubbing equipment. The high estimate gives an allowance for parasitic losses that could be experienced in the power cycle or chemical production process.

Table 6: Parasitic Losses of Typical Coal Power Plant

	UNITS	400MW - Subcritical PC, Bituminous
Condensate P/P	%	0.36
Circulating Water P/P	%	0.5
Cooling Towers	%	0.72
Feedwater P/P	%	2.3
Forced Draft Fan	%	0.36
Induced Draft Fan	%	2.09
Primary Air Fan	%	0.31
Pulverizer	%	0.52
Transformer Losses	%	0.2
Fuel Handling	%	**0.13**
Ash Handling	%	**0.2**
Wet ESP for H2SO4 collection	%	**0.15**
Baghouse	%	**0.12**
FGD	%	**1.25**
Miscellaneous	%	1
TOTAL Auxiliary Power	%	10.21
Net Unit Heat Rate	Btu/kWh	9,349
Plant Efficiency	%	36.5
TOTAL Auxiliary Power (excludes emissions and fuels in bold)	%	8.36

Finally in Table 7, there is a summary of all parasitic losses. The lift elevator, and recirculation elevator parasitic loss represents the largest number on the graphs shown above for the movement of the particulate medium. The heliostat parasitic loss represents the highest parasitic loss calculated for the complete heliostat field. The controls and miscellaneous equipment represents all the remaining parasitic losses for control of the CSHSS while the allowance for losses in the production cycle estimates a potential for the chemical production cycle to have additional losses. The allowance for losses in the production cycle is only included in the high estimate of the energy payback.

Table 7: Summary of Parasitic Losses

Component	Parasitic Loss as % of energy collected
Lift Elevator	1.86%
Recirculation Elevator	1.87%
Heliostat Field	0.14%
Controls and other misc. Equipment	1.00%
Allowance for losses in Production Cycle	7.36%

4.6 Energy Payback Analysis Comparison with other Renewables

The energy payback of the Solar Power Tower was calculated using the following equation:

$$PB_{SHSS} = \frac{(E_{\text{material}} + E_{\text{construction}})}{\dot{E}_{\text{collected}}(1 - F_{\text{PAR}})} \tag{4.6}$$

where the E_{material} and $E_{\text{construction}}$ represent the energy embodiment or energy used to construct the tower, and the denominator represents the energy collected minus the parasitic loss. The units for this Payback are in kJ_{th} divided by kJ_{th} per year or an overall unit of just years. The F_{PAR} term represents the parasitic loss of the system which includes conservative estimates of the lift elevator, recirculation elevator, heliostat field and auxiliary systems.

The energy payback for the SHSS was compared to other methods of power generation in Figure 8. The energy payback ratio of various generation types was found in the literature.[15-18] Since the literature numbers calculated payback based on electrical output, efficiencies for the various generation types were found in statistics collected by the Energy Information Administration.[23] The EIA efficiency is seen in Equation 4.5 as η_{th}.

$$PB_{other} = \frac{(E_{\text{material}} + E_{\text{construction}})}{\dot{W}_{\text{collected}}(1 - F_{\text{PAR}})} * \eta_{th} \tag{4.7}$$

As seen in Figure 8, the 10 MW_{th} Concentrated Solar Power Tower (Solar Heat Supply System) has a payback period of 0.74-0.80 years which is the lowest payback period. This advantageous payback period is mostly a result of fuel cost. The fuel cost of the coal, fission and natural gas increase the payback times of these

heat generation devices significantly over the lifetime while as the Solar Heat Supply System (Solar Power Tower) has no fuel cost. It is important to understand that this fuel cost is represented by the energy that is required to obtain the fuel, not the heating value of the fuel itself. In the case of the natural gas turbine, this fuel cost is over 95% of the cost due to the processing, production, and compression for transportation. The payback time of wind and photovoltaic cells is adversely effected by a thermal efficiency of 1 being applied in Equation 4.7. Both devices are adversely affected because they are direct electrical producing devices, so the heat is produced in a very inefficient manner. If these devices are compared on electricity generation, the photovoltaic and wind would have the same payback while the other devices would be 2.5 times as high. However, this measure of payback would equate the thermal energy used in the production of the devices with electrical work generated by the devices. This is not an indication that photovoltaic cells have a very poor energy payback for producing electricity, only that they would not be well suited for producing high temperature heat. Since the photovoltaic cell had a payback above 5 years, and because of this electrical-thermal conversion, it is not shown in the graph below. The high estimate of the CSHSS makes allowances for the parasitic loss of the power cycle while the low estimate only includes the CSHSS parasitic loss.

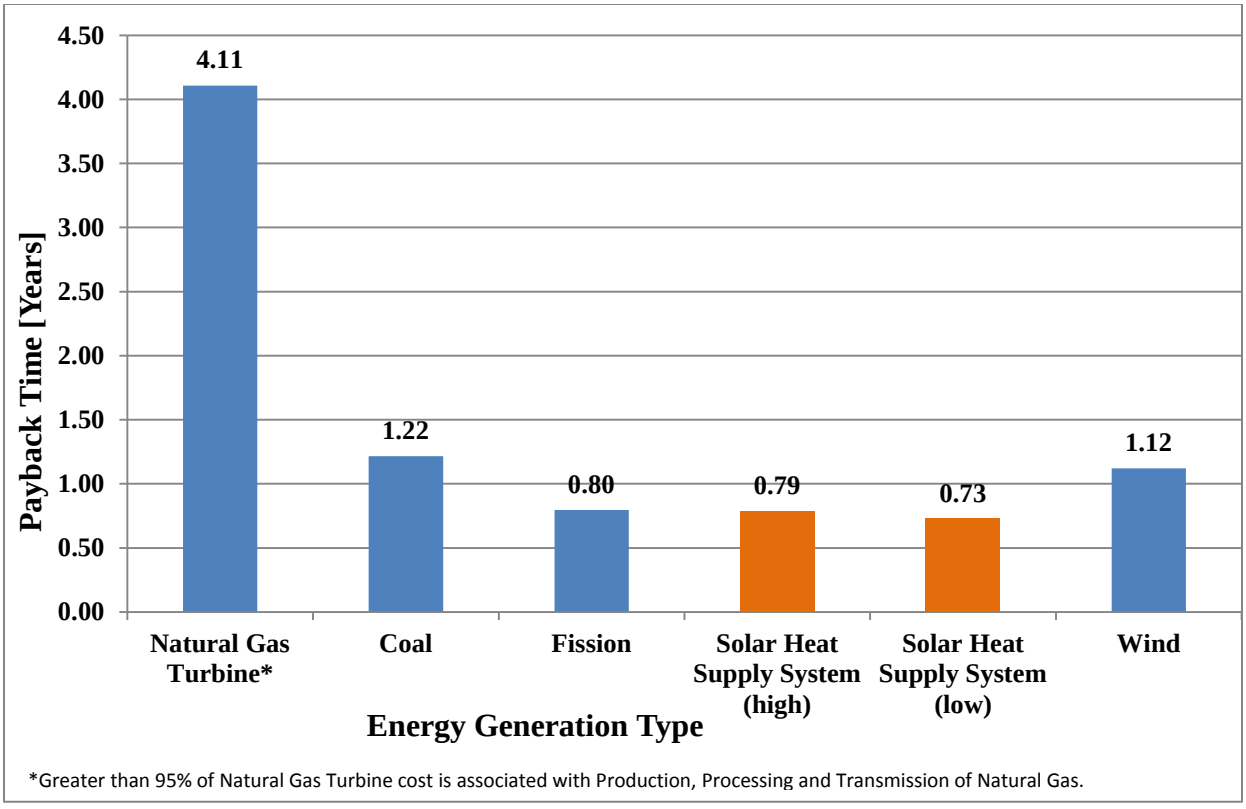

Figure 8: Energy Payback Comparison of Concentrated Solar Heat Supply System (CSHSS) to Other Energy Generation Types

4.7 Economic Analysis

The final segment of the feasibility study is the economic payback and rates of return of the 10 and 50 MW_{th} CSHSSs. The economic payback compares the capital cost of constructing a new concentrated solar tower to the savings realized by replacing only the fuel being burned in an existing combustion process. The rates of return would be much higher if the solar tower was being compared to building a new combustion process as the capital cost associated with the combustor (natural gas turbine, coal powered furnace, etc) would add to the overall savings of the solar process. The economic analysis assumes that the fuel savings are realized at the end of each year. The rate of return is calculated by comparing the present value of the capital cost of the tower to the present value of the annual annuity fuel savings. The economic payback calculates the break-even point where the initial investment is recuperated through fuel savings.

Two economic payback calculations were performed. The first economic payback uses the design of the 10 MW design to calculate the economic capital cost and compare it to the capital saved by using solar energy similar to the energy payback. The construction and materials cost were calculated and compared to the economic value of the thermal energy collected by the CSHSS. The materials were quantified based on the design, and construction costs were estimated using the R.S. Means construction data base. The overall cost of the tower, heliostat field and receiver were calculated individually. The cost of the receiver was estimated based on current research in improved receiver design. These results were compared to a SAM model of a 10 MW CSHSS. The cost of the tower was within 5% of the SAM model, the cost of the heliostat field was calculated to be about 50% of the SAM estimate and the receiver cost was also estimated to be about 50% the SAM model. This result is expected as our design incorporates a much less expensive receiver than the molten salt receiver assumed by SAM and uses an improved heliostat design. The expected heliostat cost is estimated to become about $149 per square meter. While this is above low volume prototype, it is consistent with the US DOE estimate of $125 per square meter for heliostat costs for higher volume heliostats.[30] The overall cost of the 10 MW CSHSS came to $6.8 million. The cost of purchasing fuel was used as the value of the thermal energy. Since fuel costs vary, two different energy values were used. The low energy value represents the cost of purchasing natural gas while the high energy value represents the cost of purchasing oil.[31] With a quantification of the thermal energy collected by the CSHSS in a full year, the savings of the CSHSS was calculated to be $0.37 million and $1.2 million (for the low and high energy values). Even though the savings from the capital cost required for the combustor was not included (conservative estimate), the payback period for the 10 MW tower was still 5.9 and 19.0 years for the high and low energy cost values and the rates of return were 4.3% and 17.0%. The rates of return for a 10 MW plant are both positive, and because of the economies of scale, the 50 MW will have higher returns.

The second economic analysis uses the cost calculations for a 50 MW CSHSS from SAM. The cost of the tower, heliostat field and receiver were produced by the model and are shown in Table 8. The heliostat cost is calculated by the program based on the default value of $200 per m^2 which is much higher than the cost of high volume smaller heliostats. The tower height uses an optimization program to determine the height of the tower and an optimized heliostat field layout based on the nameplate capacity of the plant. The nameplate capacity was set such that the plant would output a maximum hourly collection of 50 MW_{th} thermal. Similar to the previous analysis, the thermal energy collected by the CSHSS in a complete year was calculated and an economic

value was assigned to the thermal energy based on the cost of fuel. Again, natural gas was used as the low cost energy case and oil was used as the high energy cost case. The cost for oil was set at the recent value of $90/bbl, but due to fluctuations in the market, the savings from oil might be much higher in the future. The payback period for the 50 MW tower was 4.8 and 15.4 years for the high and low energy cost values and the rates of return were 5.8% and 21.0%. In addition to the cost savings, the CSHSS design also reduces the exposure to risk caused by price fluctuation. Since the price of sunlight is free, the cost of solar energy comes only from the collection equipment, and is not subject to fluctuations in the market. Based on the positive rate of return, the CSHSS is a cost savings design that can save money when replacing a traditional combustion process while also being more sustainable, cleaner, and lower risk due to no dependence on fuel prices. The overall results of the two economic paybacks for both the high (oil) and low (natural gas) energy values are shown in Table 8.

Table 8: Economic Cost of 50 MW CSHSS using SAM

Heliostat Field	200 59,268 $11,854,000	$/Heliostat # Heliostats
Tower	145 $8,046,000	Meters high
Receiver	44.1 $5,620,000	m^2
Total	$25,524,000	

4.8 CSHSS Feasibility Conclusion

This feasibility is a first attempt at assessing the energy and economic impact of a Solar Power Tower with thermal storage being designed at Georgia Institute of Technology. Due to the lack of actual construction data for Solar Power Towers of this design, the cost estimates are design stage, first order estimates that will need to be compared with future actual construction data. Further, the energy analysis will need to be further modified to include parasitic losses and the operation and maintenance of the tower as well as changes in the current design. An estimate of the end of life energy cost to reclaim the land is also needed. Overall, past studies have found the operation and maintenance, and end of life to be a small contribution, so the final result should not be effected much by these contributions.

The CSHSS is feasible fuel-free clean energy technology based on the energy and economic analyses and current ongoing work on CSHSS technology. The energy analysis shows that the CSHSS has an energy payback period better than coal, nuclear, natural gas and coal when including the materials, construction and operation costs of these energy conversion devices. Both economic paybacks show a positive rate of return for both natural gas and oil, and when the 50 MW power tower is compared to oil as the energy being burned, the rate

of return is over 20%. These rates of return are based on the scenario of replacing an existing combustion process. When considering building a new heat supply system (expansion or replacement of retired heat generation plant), the CSHSS would have a much higher rate of return compared to a traditional combustion process because the rate of return would be based on the capital cost savings of the combustion hardware in addition to fuel savings (this payback is based on only fuel cost savings). In addition to its very positive energy and economic paybacks, the new CSHSS technology has been proven functional in numerous projects across the world. Plants such as solar one and solar two have given way to industrial plants such as the Sierra Suntower currently operating in California and several plants operating in Spain. Additionally, other ongoing projects seek to increase the installed capacity for electricity generation in both Spain and the American southwest including the 400 MW Ivanpah project and projects by Abengoa Solar.[32] Also, the CSHSS is an environmentally friendly and sustainable design. The device operates by collecting sunlight from the sun and emits no emissions and requires no fuel. Overall, this technology is environmentally friendly and sustainable, economically viable, has a very positive energy payback, and should see expansion as a new technology.

5. Iron Ethylene Chemical Process

5.1 Ethylene Production

Heat is required for two parts of the traditional ethylene production process. First, heat is required in the production process. The reaction requires heat because the ethylene reaction has a positive change in enthalpy (endothermic reaction). In addition, heat is required to raise the temperature of the reactants from room temperature to the reaction temperature. Second, the separation process requires heat to separate the ethylene from the other products. This is done through a distillation process that takes advantage of the different phase transition temperatures of the various chemicals. For the proposed plant design, thermal energy will be collected from the solar plant and stored in sand. From there, a heat exchanger will be used to transfer the heat to the ethylene and iron processes. The use of steam as a working medium between the sand and ethylene or iron process is also a viable option for thermal energy transmission that could allow for easier integration of the different systems. Once the heat is transferred to the ethylene process, ethane will be preheated and then reacted to form ethylene and hydrogen. This reaction can be seen in Equation 5.1. Other byproducts will also be formed such as unprocessed ethane, and methane. The unprocessed ethane, once separated, can be recirculated to prevent waste. The hydrogen can be separated via membrane separation which will require a small amount of work, but will eliminate the necessity for heat input in the separation process. Once separated, the hydrogen can be delivered to the iron reduction process.

$$C_2H_8 \rightarrow C_2H_6 + H_2 \tag{5.1}$$

As mentioned, membrane separation will negate the need for the large quantities of thermal energy that is required in current industrial separation processes. The relatively small size of the hydrogen molecules compared to other products in the stream makes membrane separation more feasible. The pure, high temperature hydrogen can be used to reduce the iron ore into iron at much lower temperature than the current direct reduction methods, while keeping the same benefits of the direct reduction process. The already high temperature hydrogen will also reduce the energy input by reducing the thermal energy needed for the preheating stage. The utilization of the high temperature hydrogen prevents the waste of useful thermal energy that can be conserved and stored for production during night hours.

5.2 Iron Production

The iron ore reduction process can utilize hydrogen as a reducing agent instead of using carbon dioxide. The stoichiometric equation for iron reduction with hydrogen is shown in Equation 5.2. As with the ethylene production, this is an endothermic reaction which requires heat from the CSHSS. The expected products from this reaction include hydrogen, water, iron metal and several iron oxides including magnetite (Fe_3O_4), hematite (Fe_2O_3) and ferrite (FeO). With exception of the water and hydrogen, all of the products will be in the solid phase and the iron will need to be separated from the unprocessed iron ore and other iron oxides. A potential separation process could use a conventional method that uses Iron's lower melting temperature. The products

could be reheated to melt the iron ore and the liquid iron could easily be separated from the other solid products. The iron reduction process will obtain the needed thermal energy input from the CSHSS via sand or steam as with the ethylene production process.

$$Fe_2O_3 + 3H_2 \rightarrow 3H_2O + 2Fe \quad (5.2)$$

The most developed current process for creating iron uses the direct reduction of iron from iron ore.[33] The process mixes iron ore and coal in a single chamber combustor. The coal is partially combusted to create carbon monoxide and heat. The carbon monoxide acts as a reducing agent to reduce the iron ore into iron at high temperature (~1400-1600°C) while also producing carbon dioxide. This process has the advantage over the hydrogen based method of being a simpler process and having lower capital costs then past designs. However, the direct reduction process (along with all previous processes) also produces slag and inadvertently produced coke resulting from the use of coal. The coking causes large buildups that require the plant to be shut down for maintenance. A similar process that uses hydrogen to reduce the iron ore would have all the advantages of the direct reduction process, but would have many added benefits. Using the proposed plant design utilizes lower reaction temperatures (as low as 500-600°C), which allows less costly materials to be used and increases the plant life. Since coal is no longer required for the iron reduction process, coking and slag will no longer be of concern, the maintenance time and cost of cleaning the iron production equipment will be eliminated. The use of the solar energy as the thermal energy input also prevents the necessity for expensive combustion exhaust scrubbing equipment that may be necessary depending on local laws and regulations. The inherent clean nature of the process also provides a marketing advantage over other ethylene and iron reduction producers that utilize the current fossil fuel dependent processes. The cleaner production method would allow the producer to market the products as ‘green’ and ‘eco-friendly’.

The direct reduction of iron ore using hydrogen has been successfully demonstrated and has been proposed as a cleaner, less maintenance intensive, lower temperature alternative to the use of coal.[34] However, the proposed system has not been adopted by industry because a source of hydrogen is generally not available. In this situation, hydrogen is created in the ethylene process which can be readily used in the reduction of the iron. Alternatively, if only a decouple iron process was desired hydrogen could be produced using solar thermal energy and a small amount of methane in the well-developed steam methane reformation process discussed earlier. With a secure supply of hydrogen, the hydrogen and iron ore can be mixed and heated with thermal energy supplied by solar thermal storage to create iron through the endothermic reduction reaction in Equation 2. Because the temperature of this process is much lower, the iron will be created in the solid phase. The separation of the iron from the iron ore could incorporate the use of further concentrated solar heat to melt the iron, but may not be required based on the design of the reactor. Based on reactor design, iron purities approaching completely pure iron may be possible.

5.3 ASPEN PLUS Model

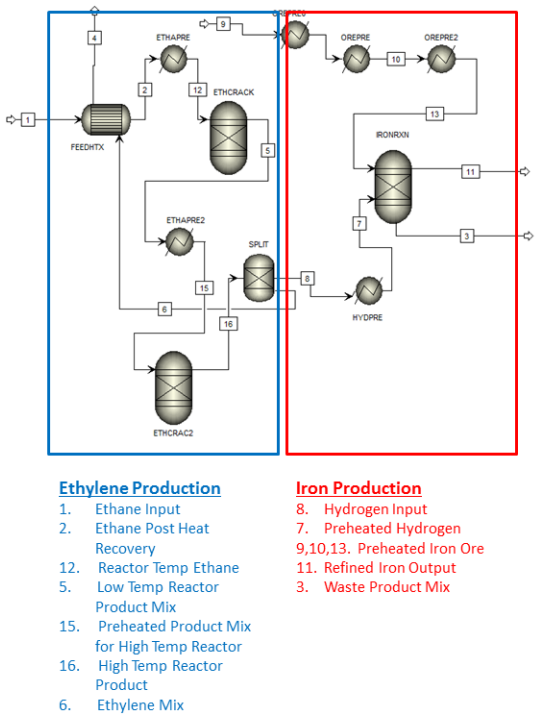

Figure 9: Aspen Diagram with Multiple Step Reactor and Preheater

A thermodynamic model of the Iron-Ethylene production process was developed using the ASPEN PLUS software. The cycle includes the preheating of each component, reactions assuming thermodynamic equilibrium is achieved and a separator assumed to be a membrane separation. A visual overview of this cycle can be seen in Figure 9. The heat input will be used at several locations in the production process. First, the ethane is preheated in the ETHAPRE component. Next, the ethane is reacted to produce ethylene and hydrogen in the ETHCRACK component. This reaction can be separated into several reactors at increasing temperature. Here it is shown as a two-step reaction. Separating the reaction into a multiple step reaction is important for creating an optimal heat rate vs. temperature diagram. The ethylene and hydrogen are then separated via a high temperature membrane. Such technology has yet to be commercialized, but research is sufficiently advanced that it would not be unrealistic to assume this technology will soon be available.[35] After separation in the SPLIT component, the ethylene can be sold and the hydrogen can be heated in the HYDPRE component before being transferred to the iron production process. With the addition of additional heat to heat the iron ore and fuel the reaction, the hydrogen can reduce the iron ore in the IRONRXN to produce water and iron. Similar to the ethylene process the solid iron will need to be separated from the other products of the reaction which given the design of the apparatus, may only require the separation of iron from the water and hydrogen (a very simple separation).

To verify the validity of the ASPEN PLUS model, a verification code was created using the Engineering Equation Solver Software (EES). This software is similar to MatLab in equation structure, but aids in the

calculation of thermodynamic data (enthalpy, entropy, etc.) for any defined state. This code essentially solves the set of iterative equations derived from the hand calculation of the thermodynamic equilibrium including the mass balance equations and the Gibbs free energy of the mixture equal to zero. The code was simplified to include only Fe, Fe_2O_3, H_2, and H_2O as possible products. The code was run for several different temperatures from 300 to 1200°C for 33% excess hydrogen. Similarly, the ASPEN results for several temperatures were recorded for comparison. The result of the Fe production is shown below in Figure 10.

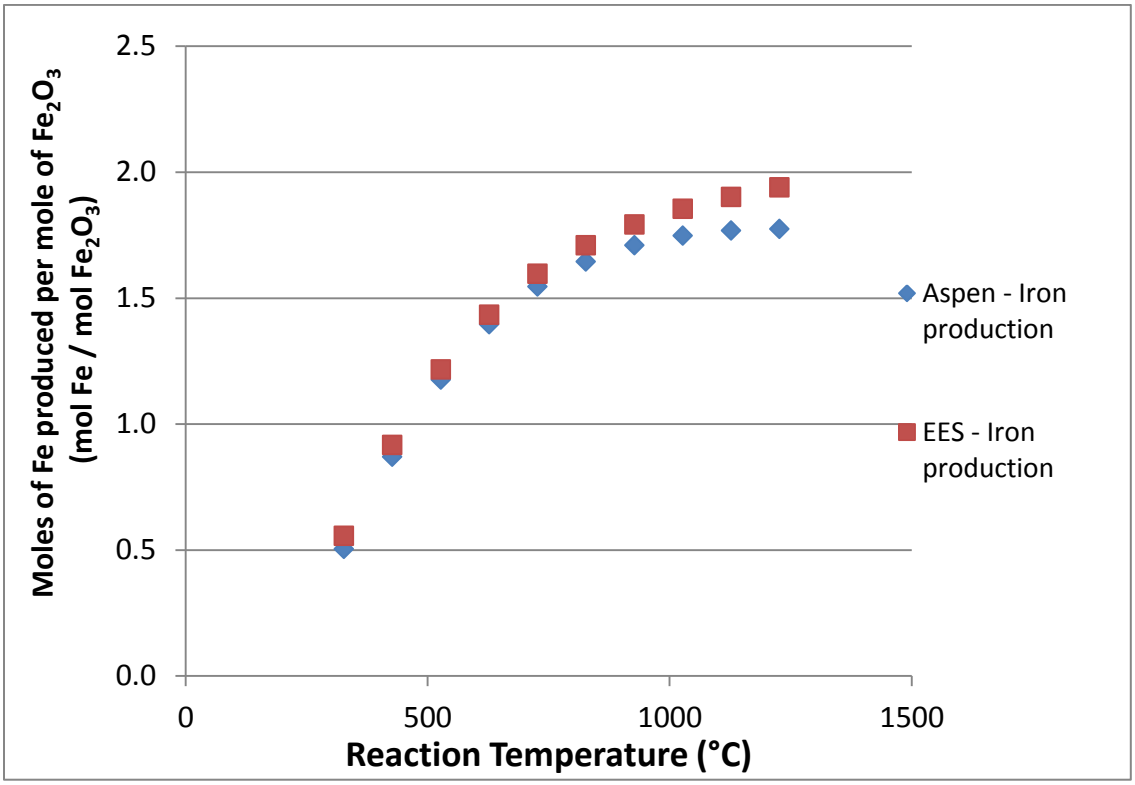

Figure 10: Thermodynamic equilibrium verification EES vs. ASPEN

Figure 10 shows the trend of the iron production calculated by the ASPEN software, and the iron production estimated by solution of the iterative thermodynamics equations using EES. Both solution methods are very close to the same production for lower temperatures, but at higher temperatures they diverge slightly. This is most likely due to slight differences in the thermodynamic data tables at the high temperatures of 900°C or higher. Overall, the production begins to level off and reach a maximum at 1200°C near the maximum production of 2 moles of iron per mole of iron ore input. The figure also indicates a confidence in the ASPEN results, although the results may be slightly underestimating iron production.

5.4 Estimated Iron and Ethylene Production

Based on the ASPEN model, the estimated production and consumption of ethane, iron ore, iron, ethylene, and water was estimated. The production rate was scaled to the heat input for a 50 MW solar thermal tower for Riyadh, Saudi Arabia using the results obtained in the solar feasibility section. Several schemes were considered for the estimation of the production. First, the temperature of the ethane and iron reactors needed to be decided. Plotting the thermodynamic equilibrium versus temperature for the two processes shows that the iron reaction is optimal around 1200°C while literature indicates a temperature around 850°C for the ethane reactor.[36] Next, the ASPEN diagram was modified to include some heat recovery as shown in Figure 9. Although additional heat recovery is possible from the iron products, the software had difficulties with the solid products in the heat exchanger. Additionally, the unique nature of the solid iron to solid ore heat exchanger may be difficult on physical constraints especially with iron quench requirements. The next important consideration is the recirculation of products. This includes the separation of the ethane and hydrogen from the products to be reused in the reactor. While the hydrogen can easily be separated from water vapor with a condenser, the ethane is more difficult to separate. Some separation technique will need to be utilized to separate the ethylene from the other products already, so adding an ethane separator should not add an insurmountable amount of added complexity. Also, the savings of ethane should more than pay for the capital cost of the equipment over the lifetime of the plant. Due to these considerations, the recirculation of ethane and hydrogen was assumed for both the ethane and iron reactions. With these assumptions, the production of each reactor was calculated separately.

First, the ethylene production rate was estimated with ASPEN based on the thermodynamic equilibrium of the products. The ethylene reaction was set to 735°C, and the thermodynamic equilibrium for the various products was calculated given the reaction temperature. This production does not consider the effects of kinetics, and assumes the reaction to be relatively fast to allow complete conversion. 0.45 moles of ethylene (C_2H_6) are produced per mole of ethane (C_2H_6) input. The production calculation was extended to find the economic value of the products. Based on the heat requirements of the ASPEN model, the production was scaled to meet the heat produced by a 50 MW CSHSS. Based on the ethylene production rate for a 50 MW CSHSS, the net profit (products-inputs) for the production process was calculated. A price of 0.68 $/lb[37] was used for ethylene, and a price of 5 $/Mmbtu[38] was used for ethane. The overall revenue of ethylene for the recovery case (not including capital cost and labor) came to 48 million USD/year while expense of purchasing ethane came to 8.5 million USD/year (or 18 million USD/year without ethane recirculation), leaving a net profit of 39.5 million USD/year with recirculation of the ethane. Note that the ethylene production is constrained to produce the hydrogen necessary to run the iron process. No attempt was made to estimate the capital cost of the ethylene plant because application of historical data would not capture major design changes of the reactor coupled with CSHSS, such as the reduction in separation equipment.

The second part of the production estimation was the estimation of iron production. The iron reactor was set to a temperature of 895°C based on the design requirements of the CSHSS. Although the calculation of the production for the ethylene can be calculated using a simple thermodynamic equilibrium, the iron reactor is not as simple. This is because the reaction includes both vapors and solids. This allows the solid and vapor phases to be easily separated. This separation can cause added production due to Le Chatelier's principle. By

removing the concentration of the end product of water from the reaction, the back reaction can be slowed, and a higher yield of iron can be realized. In fact, a device that produces near pure iron has been conceived. It requires a condenser to remove water, but could theoretically allow for the complete conversion of the iron, by removal of the water and recirculation of the hydrogen. Because of this phenomenon, the iron production was calculated using the assumption of complete conversion, and the assumption of thermodynamic equilibrium. The complete conversion represents the production if a continuous device with removal of water and recirculation of hydrogen is employed, while the thermodynamic equilibrium represents a batched process. The production was again scaled to a 50 MW CSHSS.

The production calculation was extended to find the economic value of the products. Based on the iron production rate for a 50 MW solar power tower, the net profit (products-inputs) for the iron production process was calculated. A price of 500 $/ton[39] was used for iron, and a price of 120 $/ton[40] was used for iron ore. The overall revenue of iron for the thermodynamic equilibrium assumption (not including capital cost and labor) came to 7.6 million USD/year while expense of purchasing iron ore came to 5.2 million USD/year, leaving a net profit of 2.3 million USD/year for the iron process. When moving to the complete conversion assumption, the iron revenue doubles, but the iron ore cost also doubles resulting in a doubling of the overall profit to 4.6 million USD/year. Again, no attempt was made to estimate the capital cost of the iron plant because there is very limited cost data on industrial sized iron plants using hydrogen as the reducing gas. Prediction using current plants would not accurately capture the cost improvements of a new plant.

The overall results of the complete production are shown in Table 9. In this table, the profits of both the iron and ethylene processes are shown. The ethylene process produces significantly more revenue than the iron process. Reasons for this could include the higher price for the end ethylene product compared to iron, and higher relative production of ethylene compared to iron in the process due to the required hydrogen of the iron cycle. If a lifetime of 35 years is assumed, the total revenue (again not including capital cost, and operating costs) comes to about 1.5 Billion USD. To put this in comparison to the expense of the CSHSS, the estimated cost of the CSHSS as calculated in the feasibility study above (section 4) comes to about 25 million USD. These numbers only show the potential revenue stream. Many costs including the capital cost of the Iron and Ethylene plant, Operation costs, Maintenance costs, etc. are not known. The capital cost of addition equipment such as heat exchangers and pulverizes for the iron ore are also not included. However, the numbers show the potential for the chemical cycle to be very profitable. Further development of the plant design will allow for a more accurate calculation of the costs.

Table 9: Production of Iron and Ethylene

Constants		
Molecular Weight	55.8	Kg Fe/kmol Fe
	160	Kg Fe2O3/kmol Fe2O3
Price of Ethylene	42.0	$/kmol
Price of Ethane	7.4	$/kmol
Price of Iron	500	$/ton
Price of Iron ore	120	$/ton

	Amount Produced/Consumed	**Thermodynamic Equilibrium**	**Complete Iron Conversion**
Potential Revenue	Iron (tons/yr) / Ethylene (kmol/yr)	$/year	$/year
Iron	15,120	7,560,238	14,680,074
Ethylene	1,147,549	48,154,358	48,154,358
Total		55,714,597	62,834,432
Cost of Goods Sold			
Iron ore	43,158	5,178,942	10,048,393
Ethane	1,147,549	8,484,247	8,484,246
Total		13,663,188	18,532,639
Gross Profit			
Iron		2,381,296	4,631,681
Ethylene		39,670,112	39,670,112
Total per year		42,051,408	44,301,793
Total over lifetime		$1.47E+09	$1.55E+09
Approximate cost of 50MW_{th} CSHSS	$25,500,000		
Capital Cost of Iron and Ethylene plant	N/A		
Operation, Maintenance, Cost of Capital, Other liabilities including Wages, Taxes etc.	N/A		

5.5 Proposed Research

The proposed cycle requires several research and development projects to insure its success. First, further study is needed on the direct reduction of iron ore. The current process uses coal, and although the process has been demonstrated before, studies will be necessary to both optimize the kinetics of the reaction, and assure maximum conversion. In addition, equipment development will be necessary to handle the solid

particulate and to scale production to industrial size. Current designs for both iron and ethylene production plants exist, but will need to be modified to incorporate the solar energy as the heat source. Another potential issue is the storage of the iron product. Currently, iron is stored in large ingots or rods which have a much better packing density and better resist oxidation. The small particulate may be particularly at risk of oxidation with very high surface area to volume ratios. This same problem applies to packing the particulate for transportation. The high surface area to volume ratio will cause the iron product to have a much lower packing density and thus take up more space. Finally, with the possibilities of partial reduction occurring, separation techniques may be necessary to purify the iron.

The second area of research required is in the area of hydrogen separation. The byproduct of hydrogen will need to be separated from the products of the ethylene reaction to be utilized during the iron reduction phase. This can be accomplished using a membrane separation method, but this has not been previously used in the separation ethylene products. Further, the hydrogen is at high temperature which puts added constraints on the membrane separation process. Although the small size of the hydrogen molecule compared to the other molecules makes it conducive to separation, further research will be needed to assess both technical feasibility with the high temperature constraints and economic feasibility of this process. Alternatively, the developed processes of distillation can be used.

The biggest difference between the proposed plant design and current industrial processes is the method of power input for the endothermic reactions. Using solar energy provides several benefits, but to realize the maximum potential of this resource, more work must be done to create the most reliable, efficient, and cost effective concentrated solar tower. One critical area of focus is the solar receiver. Most receivers use molten salts as the working fluid, but the proposed design will utilize sand to capture the thermal energy. Using this as the working fluid will allow for the use of less expensive materials which will create a significantly cheaper receiver. With this change we predict it is possible to construct a receiver at less than 50% the cost of current comparable receivers. Improvements that have been made to the heliostat design and field layout will contribute to the extensive cost reductions expected by further research. Continuing the development of the plant will allow us to generate more accurate cost estimates for construction.

In addition to the improvements necessary in the solar thermal collection equipment, improvements in the equipment necessary for handling, storing and moving the thermal energy stored in a particulate is necessary. Adequate handling equipment for the working fluid will have to be acquired or constructed, but will not have the high demands and expense as the high temperature, high pressure piping and storage of molten salt storage. Tower construction costs can be significantly reduced by using sand as the working fluid throughout the system due to the lower grade of materials that can be utilized. In addition, the sand handling equipment is can use innovations developed for the handling of other granular materials. The concepts from other predesigned granular material handling equipment can be readily adapted to this situation.

6. Exergy Analysis

An Exergy analysis is the process of determining the potential work of a system, and the potential work destroyed at every stage of the process. This is done by a combined 1st and 2nd law thermodynamic analysis that quantifies the theoretical amount of useful work that could be generated by the stream if it were brought to the conditions of the reference medium. The reference medium is generally assumed to be the conditions of the atmosphere at standard temperature and pressure (STP). This potential work can be stored as thermal mechanical exergy or as chemical exergy. Thermal mechanical exergy stores work in the form of enthalpy differences and/or pressure differences while chemical exergy stores potential work in chemical bounds of molecules.

This system is still in the theoretical stage of development meaning several design variables could change. Rather than focus on the absolute exergy values for the actual system, this section makes a best guess for these design variables (especially the size of the plant) and focuses on the methods required to calculate the exergy of the system. The temperatures of the reactors will cause large changes in the extent of reaction and as a result changes in hydrogen concentration, changes in required compressor work, and heat input for the hydrogen heater. Also, the ratio of hydrogen produced to the iron ore input will make changes to the iron reaction. Because of these possible future modifications, the exergy numbers are not applied to the overall system as addition parasitic costs or any other implications. Future work will continue to optimize the system for efficiency and output. These modifications can later be updated in the exergy analysis according to the methods developed here to find the updated exergy values.

6.1 Exergy Theory Introduction

In any design stage analysis, finding the efficiency of the process is important. It is important to know how much product will be produced at what cost. Several different measures exist for determining the efficiency of each component in a process, but the best measure is generally a measure of the exergy of the system (also known as the availability). Most measures of efficiency only include the 1st law energy balance and ignore the very important 2nd law considerations. On the other hand, the 2nd law entropy analysis normally yields results that are hard to interpret and apply to an actual physical system. An exergy analysis combines both the 1st and 2nd laws to allow for complete and intuitive efficiency results. The exergy analysis finds the theoretical maximum amount of work that can be produced by a given stream and a reference medium (usually taken to be the atmosphere). This theoretical maximum amount of work called the “stream exergy” can then be used to find the amount of potential work destroyed by each process. This potential work destruction, called the exergy destruction, can be related to the entropy generation of the system and indicates the loss or inefficiency of a given component.

The derivation of the exergy equation includes two main parts: the thermo-mechanical exergy and the chemical exergy. The thermo-mechanical exergy includes all of the pressure and heat exergy of the system i.e. all of the work that could be generated from heat and pressure differentials. The chemical exergy includes all of

the work that can be produced through a chemical reaction. For example, in a fuel cell, H_2 and O_2 are reacted to generate electrical work and H_2O. The theoretical development for both the thermo-mechanical and chemical exergy is explained in the next.

First, the thermo-mechanical exergy can be found by combining the 1st law shown in Equation 6.3 with the 2nd law shown in Equation 6.4. In these equations, both the heat rate, $\dot{Q}$, and the net-work, $\dot{W}$, use the convention of in being positive, but include energy flow both into and out of the control volume.

$$\frac{dE}{dt} = \sum_{in} \dot{m} H_{\mathrm{GT}} - \sum_{out} \dot{m} H_{\mathrm{GT}} + \sum_{i=1}^{n} \dot{Q}_{\mathrm{in},i} + \dot{W}_{\mathrm{in}} \tag{6.3}$$

$$h_{\mathrm{GT}} \equiv h + \frac{V^2}{2} + gz \tag{6.3b}$$

$$\frac{dS}{dt} = \sum_{\mathrm{in}} \dot{m} s - \sum_{\mathrm{out}} \dot{m} s + \sum_{i=1}^{n} \frac{\dot{Q}_{\mathrm{in},i}}{T_i} + S_{\mathrm{gen}} \tag{6.4}$$

The goal of combining the two equations is to find the maximum amount of useful work available in any given arbitrary stream. Again, for the thermo-mechanical exergy, the stream has the restriction of no chemical reaction occurring. First, recognize that the useful work does not include any work on the medium by expansion of the control volume as shown in Equation 6.5. This causes $\dot{W}_{in}$ to be modified by $P_o \, dV/dt$. Then, Equation 6.6 can be found by multiplying the entropy equation by the temperature of the medium, T_o, and adding the energy equation. The final result shows the actual useful thermo-mechanical work available in a stream. Also, the S_{gen} term is defined as $\dot{I}$, the exergy destruction.

$$\dot{W}_{\mathrm{use}} = \dot{W}_{\mathrm{in}} - P_o \frac{dV}{dt} \tag{6.5}$$

$$\dot{W}_{\mathrm{act,use}} + \frac{d(E + P_o V - T_o S)}{dt} = \sum_{\mathrm{in}} \dot{m}(h_{\mathrm{GT}} - T_o s) - \sum_{\mathrm{out}} \dot{m}(h_{\mathrm{GT}} - T_o s) - \sum_{i=1}^{n} \dot{Q}_{\mathrm{in},i}\left(1 - \frac{T_o}{T_{\mathrm{i}}}\right) + T_o S_{\mathrm{gen}} \tag{6.6}$$

$$\dot{I} \equiv T_o S_{\mathrm{gen}} \tag{6.6b}$$

To find the goal of the maximum possible work that is available in the stream, we assume the process to be internally reversible and setting S_{gen} equal to 0. This reduces Equation 6.6 to the stream exergy of the system shown on the right hand side.

The chemical exergy is found by relating the chemical potential of the stream to the chemical potential of the medium. This exergy finds the available work of a system caused by a chemical reaction. For example, a fuel cell generates electrical work completely from the available chemical exergy stored in the inlet hydrogen and oxygen. The chemical exergy is found by finding the chemical potential of the stream at the temperature and pressure of the medium (the "frozen dead state") and comparing it to the chemical potential of the medium. It is also important to remember that the stream can contain multiple chemical species, so the chemical exergy of each chemical species will need to be calculated and summed to find the chemical exergy of the entire stream. Equation 6.7 shows the complete stream exergy of the system. In Equation 6.7, the properties have been switched to molar properties to avoid complicating the equation with multiple molecular weights, and the chemical exergy of the medium has been added to the thermo-mechanical exergy from Equation 6.6. Here, the reference state of the thermo-mechanical exergy for the enthalpy and entropy is assumed to be the same as the frozen dead state, allowing them to cancel. It is important that a consistent reference be used for both the frozen dead state and the reference relative dead state or else Equation 6.7 becomes longer and more complicated than the simplified form shown here. Also, for our system, we are assuming a steady state problem which eliminates the transient derivative on the left hand side. Finally, to find the maximum possible reversible work, the exergy destruction must be equal to zero.

$$\dot{W}_{\text{act,use}} = \sum_{\text{in}} \sum_{k} \dot{N}_k (\overline{H}_{\text{GT,k}} - T_o \overline{S}_{\text{k}} - \mu_k^0) - \sum_{i=1}^{n} \dot{Q}_{\text{in,i}} (1 - \frac{T_o}{T_i}) \tag{6.7}$$

For any chemical species that exists in the medium, the chemical potential of the medium can easily be found by finding the molar Gibbs property. However, species such as ethane (C_2H_6) have no component in the medium and thus require a different method to find their respective potential. The μ_k^0 of any chemical species not present in the medium is considered to be a "fuel" and requires the calculation of the "fuel exergy". The chemical potential of these species is found by finding a system of chemical equations that relates the "fuel" to the chemical species in the atmosphere. For example, ethane can be related to the species in the medium (O_2, H_2O, CO_2) through its combustion reaction. The generalized fuel exergy is shown in Equation 6.8. For more in-depth development of the exergy equations see Wark chapter 3.[41]

$$\mu_{\text{fuel}} = (-\mu_{R1}\upsilon_{R1} - \mu_{R2}\upsilon_{R2} - \cdots + \mu_{P1}\upsilon_{P1} + \cdots) \tag{6.8}$$

6.2 Exergy Analysis-CH_4 Combustion

These exergy equations were used in conjunction with the ASPEN PLUS model to develop an exergy model including the stream exergy of each stream and the exergy destruction of each component. To validate both the results from ASPEN and the exergy calculations, a simple methane combustion model was developed using both the ASPEN PLUS software and using hand calculations solved with Engineering Equation Solver (EES). A schematic of the model is presented below in Figure 13.

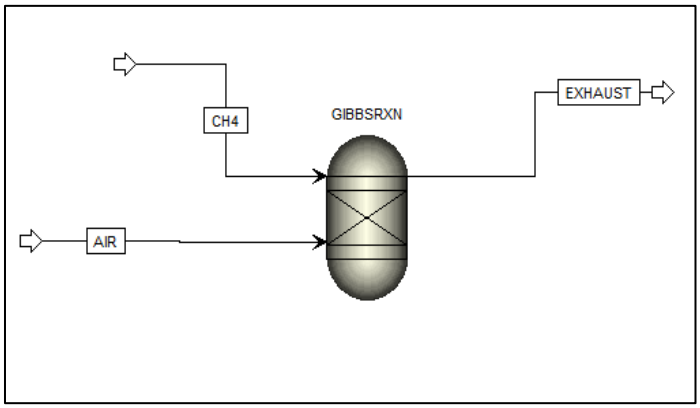

Figure 11: CH4 Simulation Diagram

To model the methane combustion process, a simple Gibbs reactor with two separate inlets was utilized. The model has two inlets: the air stream containing pure oxygen with 0.5 excess oxidizer, and the fuel source of pure methane. Both inlets were at the reference temperature of 298K, the reference pressure of 1 bar, and in the vapor phase. The reactor was set to operate at 1000K. The exit stream left the system at the reactor temperature and with all components in the stream in thermodynamic equilibrium. The results from the ASPEN PLUS stream properties was used to calculate the stream exergy values. Using these values and the Q output determined during the simulation, the exergy destruction of the system was determined.

The two APSEN based models utilized the internal entropy and enthalpy data. The AVAIL function automatically calculates the Gibbs property (h-$T_0 \cdot s$) for each of the streams. To verify the AVAIL function, ASPEN's stream exergy function, within ASPEN PLUS we used the enthalpy and entropy values to manually determine the stream exergies. The enthalpy and entropy values were extracted from the model and the Gibbs property was calculated using simple hand calculations. These results matched the outputs from the AVAIL function for the pure substance inlet streams, but varied by around 9% for the mixed exhaust stream.

After finding the stream exergies using ASPEN, EES was used to perform verification hand calculations. The EES's internal thermodynamic data from the NIST JANAF tables was used to calculate the thermodynamic equilibrium, the Gibbs property, the Q exergy, the g_{medium}, and the overall stream exergy of each stream. All the components of the exergy analysis were calculated with two separate versions of code to verify the accuracy of the calculations. Both of the EES codes yielded the same results within a small margin of error. This yielded four separately derived sets of data: two from the ASPEN software, and two from the EES code. The stream exergy between the four models was compared with our previously verified EES model we calculated the difference between each model. Table 10 presents our results from this simulation.

This agreement between models indicates that ASPEN PLUS's internal entropy and enthalpy functions were working properly and gave us confidence that we had the correct process to determine the stream exergy. This calculation process could then be applied to the much more complicated Iron-Ethylene production process.

The more complicated Iron-Ethylene process would create addition problems due to the multiple phases, multiple components and mixed stream states, but this model allowed for the solution of many issues with the software and calculations before dealing with the larger process.

Table 10: CH4 Simulation Results

Exergy	Units	Aspen AVAIL	Aspen H-ToS	EES 1	EES 2 (JT)
O2 Stream	kJ/sec	11,861	11,861	11,867	11,867
Fuel Stream	kJ/sec	829,696	829,718	829,615	829,615
Exhaust Stream	kJ/sec	130,005	120,230	119,731	119,835
Q exergy	kJ/sec	-494,776	-494,776	-494,681	-494,861
Exergy Destroyed	kJ/sec	216,776	226,573	226,971	226,966

6.3 Stream Exergy Analysis-Iron Ethylene Process

The process learned through the simple methane combustion process was then applied to the more complex Iron-Ethylene production cycle. The stream exergy of each stream was calculated by finding the Q exergy, Gibbs free energy of each component in the medium, the total molar enthalpy, and total molar entropy assuming a steady state system. The stream exergy was calculated using three different methods to verify the results. The first method simply uses the enthalpy and entropy given in the results table of ASPEN to calculate the stream exergy. The second method uses the ASPEN AVAIL function. This function is a supposed short-cut that calculates $h\text{-}T_oS$ directly. Finally, the enthalpy and entropy of each stream was calculated using the mole composition of each stream provided by ASPEN and an interpolation of the enthalpy and entropy at the given pressure and temperature provided by the NIST JANAF thermochemical data.[42] Inconsistency in the ASPEN AVAIL function was noticed for streams with multiple chemical species and thus produced invalid results. Good agreement between the JANAF and $H\text{-}T_oS$ results was achieved.

The complex nature of the system required that special attention be given to the phase related options within ASPEN. First, the equation of state for the entire process was selected to be the SRK model. The output was compared to the output for the WILSON equation of state, and no noticeable difference in the properties was observed. Next, ASPEN requires that the phase be specified in both the block and the stream (the phase is specified twice). In addition, it is not recommended to use the option allowing ASPEN to determine the phase. When using this option, the ASPEN software caused inappropriate phase changes that resulted in entropy values defying the 2nd law. These component blocks also had a difficult time analyzing the mixed state streams. On several occasions the presence of solids in a vapor stream skewed the results dramatically. To overcome this

pure state streams were used with the assumption that phases would be separated within the reactor with no additional energy input.

Three main components were calculated to find the stream exergy of each stream. First, the H-T_oS part was calculated as the total molar properties of the stream. This was done as a weighted molar average of each chemical species. Next, the Q exergy was calculated. The Q values were calculate using the 1st law balance on each component, and were compared to the Q values calculated by ASPEN as shown in Table 11. The Q values were very close and only differed by a small margin. The FEEDHTX and SPLIT had large percent difference, but this is due to the small magnitude of the numbers. All of the preheaters were modeled as reversible heat input. The effective temperature of heat input was calculated as the change in enthalpy divide by the change in entropy. This caused all of the preheaters to be completely reversible and as expected, they had an exergy destruction of zero. Finally, the g_{medium} (or μ_k^0) was calculated using the enthalpy and entropy of each component. A medium composition was devised that uses the mole fraction of the gases in the atmosphere and assumes Fe_2O_3 to be present as a solid in the medium. The g_{medium} of each of these components was calculated and used to find the fuel exergy of Fe, C_2H_4, H_2, and C_2H_6.

Table 11: 1st Law Energy Balance

1st Law Energy Balance (H-T_oS)			
Component	**Qin=H_{out}-H_{in}-Win kJ/sec**	**ASPEN Q kJ/sec**	**% difference %**
ETHAPRE	188721	188721	0.00
ETHCRACK	314720	314720	0.000
FEEDHTX	-0.0410	0.00	-100
SPLIT	-14.2	-14.2	-0.2
HYDPRE	-14673	-14673	0.000
OREPRE	133821	133821	0.00
IRONRXN	20364	20364	0.001
COMPRESS	0	0	0.000

6.4 Results of Stream Exergy Analysis

Figure 12 shows the results of the stream exergy analysis. Notice that this figure incorporates a compressor that is not included in the other models. This is to account for the compression work required to raise the partial pressure of the hydrogen stream across the separator. The stream exergies calculated using the NIST JANAF table properties and the stream compositions from ASPEN are highlighted in boxes, while the stream exergies calculated with the H-T_oS method entirely from ASPEN properties and compositions are the numbers displayed without boxes. As seen in the figure, there is good agreement between the two methods for all streams. Streams 9 and 10 seem to have very large errors, but this only due to the much smaller magnitude of the exergies at these two states. Stream 10 has the largest difference, and this is due to the thermochemical

data tables. There is a difference in the enthalpy property calculated by ASPEN and JANAF. The stream exergy calculation requires the calculation of three main components: the Gibbs property H-T_oS, the g_{medium} of the stream, and the Q exergy of the stream.

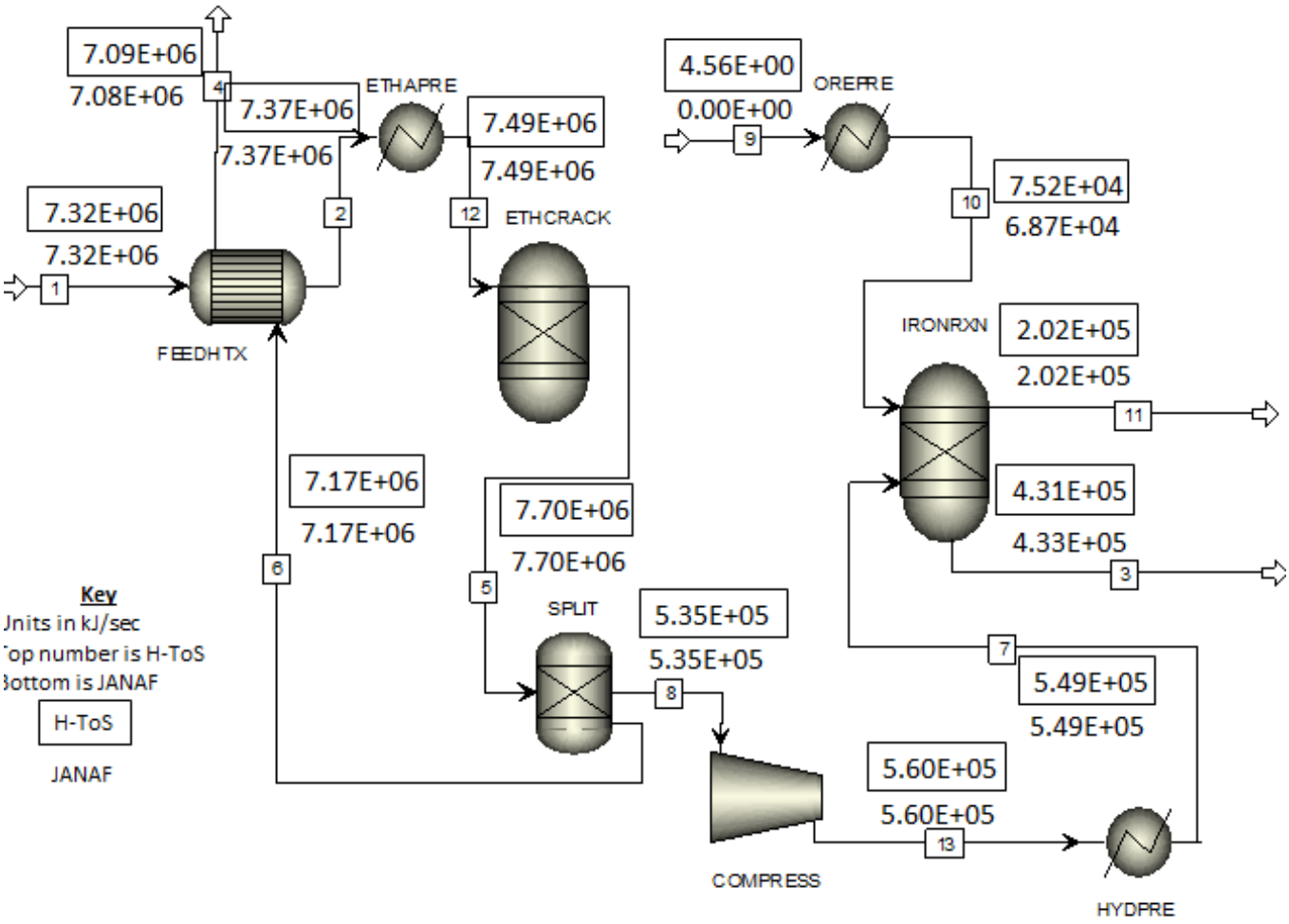

Figure 12: Aspen Diagram with Stream Exergy Results

Table 12: Medium Composition

Component	Mole Fraction	g=h-T_os (H-T_oS) kJ/kmol	RTln(P*medium/P) kJ/(kmol*K)	G=g+RTln(P*/P) (H-T_oS) kJ/kmol	G=g+RTln(P*/P) (JANAF) kJ/(kmol*K)
O2	0.203	-32.6	-3956	-3988	-65081
CO2	0.000	-394407	-19457	-413864	-476664
H2O	0.032	-228624	-8556	-237180	-306633
N2	0.756	-32.6	-693	-725	-57793
Fe2O3	1 (solid)	-742688	0.00	-742688	-851561
H2	N/A	N/A	N/A	-235186	-274093
FE	N/A	N/A	N/A	-368353	-376970
C2H6 (ethane)	N/A	N/A	N/A	-1525309	-1645445
C2H4 (ethylene)	N/A	N/A	N/A	-1290124	-1371352

The g_{medium} calculation is shown in Table 12. This table shows the composition used for the medium and the corresponding g_{medium} calculated per mole of species. The first five species are considered to be part of the medium, and the g_{medium} was calculated as the simple Gibbs property. The remaining four components were found using the chemical exergy. These chemical exergies were found through a system of four chemical equations shown below in Equations 6.9a-d.

$$2H_2 + O_2 \rightarrow 2H_2O \tag{6.9a}$$

$$Fe_2O_3 + 3H_2 \rightarrow 3H_2O + 2Fe \tag{6.9b}$$

$$2C_2H_6 + 7O_2 \rightarrow 4CO_2 + 6H_2O \tag{6.9c}$$

$$C_2H_6 \rightarrow C_2H_4 + H_2 \tag{6.9d}$$

The Gibbs property and the Q exergy were calculated using the enthalpy and entropy of each stream. The results of the Q exergy is shown in Table 13. There were small deviations between the two methods, but overall the results were very consistent. The total shows the total theoretical Q exergy needed for this process is about 447 MJ (work)/kmol iron ore input (assuming a constant ratio of ethane input to iron ore input). The hydrogen preheater is showing a negative heat input due to the compression process. This heat could be used in the reaction process to reduce or eliminate the heat needed in the reaction. Again, the heat required in the HYDPRE component will be very dependent on the extent of reaction in the ethylene reactor and the partial pressure of hydrogen output from the separator.

Table 13: Component Thermal Exergy

Component Q Exergy				
Component	**Q (H-T_oS) kJ/sec**	**Q (JANAF) kJ/sec**	**Q exergy (H-T_oS) kJ/sec**	**Q exergy (JANAF) kJ/sec**
ETHAPRE	188721	188738	120783	120805
ETHCRACK	314720	314223	221645	221294
FEEDHTX	0.00	0.00	0.00	0.00
SPLIT	-14.2	0.00	-10.0	0.00
HYDPRE	-14673	-14682	-11235	-11217
OREPRE	133821	124702	75158	68727
IRONRXN	20364	32561	15166	24250
COMPRESS	0	0	25400	25402
Total	642938	645541	446907	449262

The exergy destruction is also shown in Table 14. As expected, all of the preheaters had an exergy destruction of zero. This is due to them being modeled as reversible heat input. A future study will include a Q vs T diagram for exchanging heat between all of the components and calculate the additional exergy destruction due to the heat exchange between the CSHSS and the Iron-Ethylene production process. This will account for the heat transfer exergy destruction. Similarly, the splitter had zero exergy destruction as there is no heat input or work input required in the separation since the separator is modeled with constant partial pressures across the separation. Additionally, as expected, the heat exchanger has the largest exergy destruction due to the inherent heat transfer irreversibility. The compressor is again modeled as a reversible isentropic compression. This means the indicated exergy destruction for the compressor also is what is expected.

Table 14: Component Exergy Destruction

Component Exergy Destruction				
Component	**I (H-T_oS) kJ/sec**	**I (JANAF) kJ/sec**	**I (H-T_oS) % of Q exergy in**	**I (JANAF) % of Q exergy in**
ETHAPRE	0.00	0.00	0.000	0.000
ETHCRACK	11698	11611	0.151	0.149
FEEDHTX	34720	34794	0.447	0.448
SPLIT	0	0	0.000	0.000
HYDPRE	0.00	0.00	0.000	0.000
OREPRE	0.00	0.00	0.000	0.000
IRONRXN	6620	7182	0.085	0.092
COMPRESS	0	0	0.000	0.000
Total	53038	53587	0.683	0.690

The results for the exergy destruction were verified with a second law analysis shown in Table 15. The second law analysis calculates the exergy destruction via the entropy generation (S_{gen}) of the system shown in the bottom of Equation 6.4 above. The $T_{effective}$ of the system was calculated using the change in enthalpy over the change in entropy method. The stream entropy and Q entropy were added to find the S_{gen} of the system. The exergy destruction calculated with the exergy law and the exergy destruction calculated with the 2nd law are compared in the last column, and there is little difference between the two methods, verifying the accuracy of the model.

Table 15: 2nd Law Entropy Balance ($H-T_oS$)

2nd Law Entropy Balance ($H-T_oS$)						
Component	**Stream Sin-Sout** kJ/sec*K	**T effective** K	**Q/T** kJ/sec*K	**Sgen** kJ/sec*K	**$I=T_oSgen$** kJ/sec	**Difference in I** kJ/sec
ETHAPRE	-228	828	228	0.00	0.01	1.31E-02
ETHCRACK	-351	1008	312	39.2	11698	2.31E-03
FEEDHTX	-116	0.00	0.00	116	34720	-4.10E-02
SPLIT	0.0	1008	-0.01	0.0	4	4.19E+00
HYDPRE	11.53	1272	-11.53	0.00	0.00	3.05E-04
OREPRE	-197	680	197	0.00	0.07	7.09E-02
IRONRXN	-39.6	1168	17.4	22.2	6620	-3.23E-02
COMPRESS	0.0	0	0.0	0.0	0	0.00E+00

Finally, Table 16 shows the result of a full system analysis. It treats the entire production process as one large component and calculates the Q exergy in, the stream exergy in, the total exergy into and out of the system, and the exergy destruction. Again, the exergy destruction from this overall balance matched the totaled exergy destruction in Table 14.

Table 16: Overall Cycle Values ($H-T_oS$)

Overall Cycle Values ($H-T_oS$)		
Q Exergy in	446907	kJ/sec
Stream Exergy in	7323989	kJ/sec
Total Exergy in	7770896	kJ/sec
Total Exergy Out	7717854	kJ/sec
Total Exergy Destroyed	53042	kJ/sec

6.5 Exergy Conclusion

Although the cycle has not been optimized or scaled to a specific size, the general trends can still give insight into the behavior of the process. The stream exergies indicate that the areas of highest exergy are in the ethane cycle, and indicate a very large exergy leaving in stream 4. It will be important to find a use for this exergy in the optimization of the process either in recycling the products, or using them for another purpose. The exergy destruction of the splitter also shows the work requirement need for the hydrogen separation process. Finally, the analysis helped illuminate issues with the software program including the difficulty with the AVAIL function with mixed phase streams. As the project develops, this theoretical development can be integrated with future practical considerations (such as the efficiency of various components and cost) to make design stage estimates of production, fuel requirements, energy requirements and capital costs.

7. Heat Exchange Analysis—Heat Rate vs. Temperature Diagrams

As explained in the exergy section, the heat loss resulting from the heat exchange between the CSHSS and the chemical process is not included in the theoretical exergy analysis. In order to account for this loss, it is necessary to devise a Heat Rate vs. Temperature diagram simulating the heat exchange between the Solar Thermal Storage medium (in the CSHSS) and the various chemical processes. This diagram simultaneously simulates the heat exchange between the high temperature thermal storage medium and each of the components in the ASPEN Diagram. A minimum temperature of approach of 100°C was assumed to simulate the physical constraints of the heat transfer in the heat exchanger. The goal of producing the diagram was to minimize the exergy destruction of the process. This is done by minimizing the temperature difference between the "Sand" line representing the thermal storage medium, and the chemical process lines representing all of the processes requiring heat from the ASPEN diagram. Three heat rate diagrams were constructed: one representing a best fit for the original simple ASPEN diagram, one showing an example of an improved diagram with a much more complex ASPEN diagram, and one diagram for comparison representing the result of a simple Rankine cycle. The three cycles are compared by calculating the exergy destruction of each case.

7.1 Simple Heat Rate vs. Temperature Diagram

The first of the heat rate diagrams uses the ASPEN diagram heat requirements from the ASPEN diagram in Figure 12. In this model, heat is required for the ETHAPRE, HYDPRE, and OREPRE representing the 3 preheaters for the ethane, hydrogen and iron ore respectively; as well as, the heat required in the reactors. This includes heat from the ETHCRACK and IRONRXN components. Since the heat requirement is dictated by the first law energy balance of each of those components, the temperature vs. heat rate of each component can be plotted separately. The most important decision made was the order of the various components. The various chemical processes were fit under the sand line so that the exergy destruction and the maximum temperature of the sand line was minimized while still achieving the required temperature of approach. It was assumed that every preheater had a constant specific heat, while all of the reactors had a constant temperature heat input. The constant specific heat assumption is very close to valid for the iron ore stream, but for the hydrogen and ethane, there is significant variability. This however does not affect any of the end points of lines, but would instead make the lines slightly curved as the specific heat changed with temperature. This will have a small effect on the overall exergy destruction, but has little or no effect on the meaning of the diagram as the end points are the most important information. This is because the end points dictate the temperature of approach, and the design of the heat exchangers.

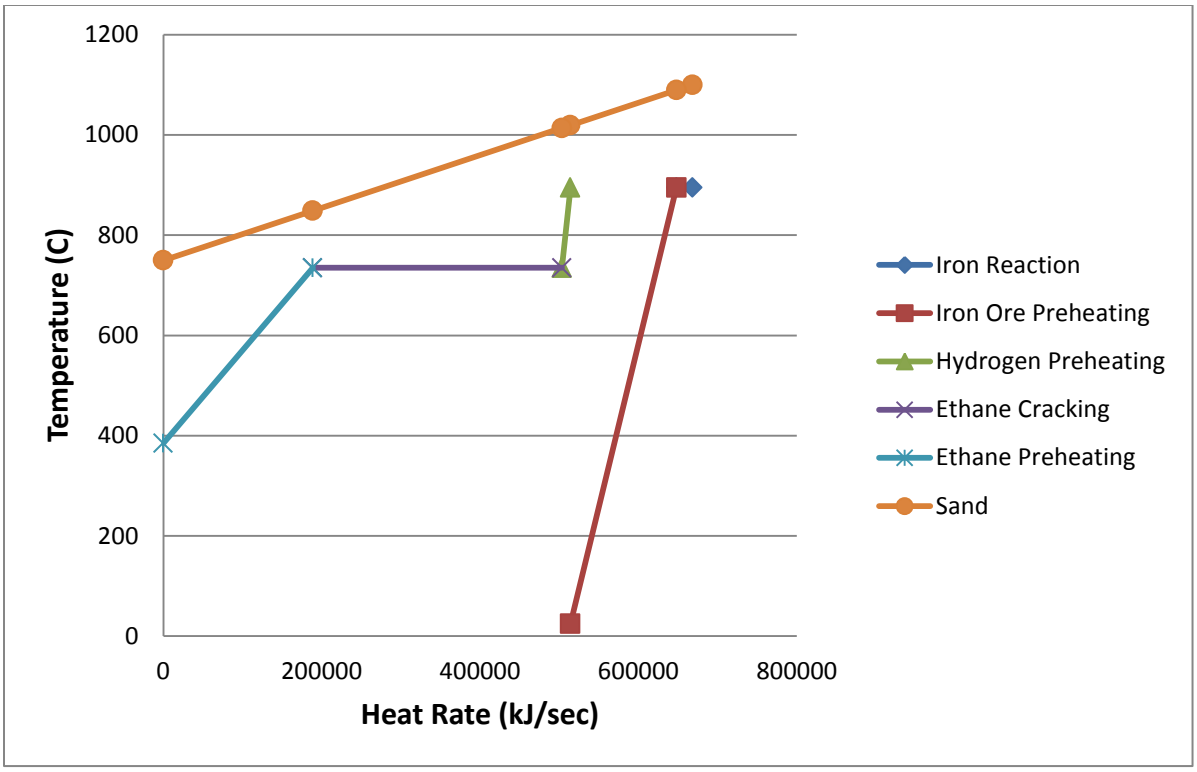

Figure 13: Simple heat rate vs. temperature for heat exchange between sand and iron-ethylene chemical process

The Heat Rate diagram shown above shows the result of the idealized heat exchange between the thermal storage medium (sand) and the various components of the chemical process from the ASPEN diagram. This diagram shows that the sand line must reach a maximum temperature of around 1100°C to meet the minimum requirement of a 100°C temperature of approach. The diagram also shows that the iron ore preheating generates a large amount of exergy due to the very large temperature difference. Table 17 below shows that the temperature of approach for the OREPRE component reaches almost 1000°C indicating a very wasteful system that will result in a large exergy destruction.

Table 17: Simple Heat Rate vs. Temperature — Q Consumption Breakdown

Component	%Q Consumed	T low (°C)	T high (°C)	Temperature of approach (°C)
IRONRXN	3.05%	895	895	205 194
OREPRE	20.02%	25	895	194 994
HYDPRE	1.60%	735	895	124 279
ETHCRACK	47.09%	735	735	279 114
QETHAPRE	28.24%	385	735	114 365

The exergy destruction results are shown in Table 18. As predicted, the large temperature difference between the sand line and iron ore preheater results in a large exergy destruction. In addition, the exergy destruction of the full process comes to about 58 MJ/sec. When compared to the total exergy destruction calculated in the section 6 of around 63 MJ/sec, we see that the exergy destruction of the heat exchange is almost as great as the theoretical exergy destruction of the chemical process. Because of this, it is important to construct a more efficient heat exchange processes. The next section deals with improving this model by using the more complicated ASPEN diagram with multiple reactors in Figure 9.

Table 18: Simple Heat Rate vs. Temperature—Exergy

Q Exergy Chemical Process			
Component	Q KJ/sec	T effective K	Q exergy KJ/sec
Sand	668342.4	1189.6	500917
IRONRXN	20363.8	1193	15277.1
OREPRE	133820.9	680.1	75187.2
HYDPRE	10723.4	1086.5	7782.3
ETHCRACK	314719.6	1033	223929.3
QETHAPRE	188714.7	828.2	120813.7
Total	668342.4		442989.5
Exergy Destruction			57927.5

7.2 Improved Heat Rate vs. Temperature Diagram

Because of the large exergy destruction of the iron ore preheating, an improved heat rate vs. temperature diagram was devised. This diagram builds upon the original ASPEN diagram by expanding the number of reactors and preheaters. This expansion allows for the previous iron ore preheater to be reordered. The low temperature section of the iron preheating can be moved to the low temperature left hand side of the diagram while the high temperature section can be kept on the high temperature side of the diagram. The full ASPEN diagram of the more complex system is shown in Figure 9. In this figure, the ore preheater is segmented into three sections, the ethane preheater is divided into two sections and the ethane reactor is divided into two sections. The high temperature iron ore preheater and hydrogen preheater are combined as a joint preheater. This causes the chemical process to be divided into a total of eight different heating components that are shown on Figure 14.

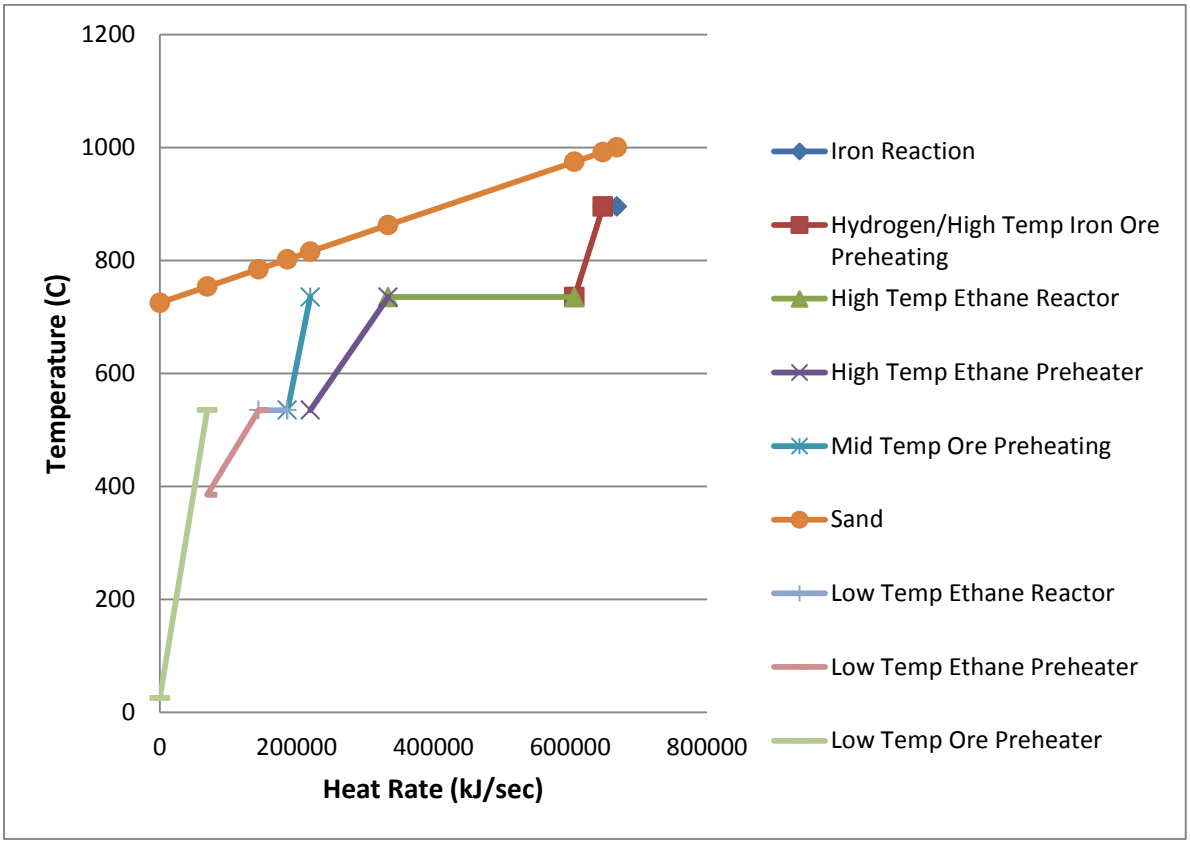

Figure 14: Complex heat rate vs. temperature for heat exchange between sand and iron-ethylene chemical process

The eight chemical process components are order according temperature to allow a best fit under the sand line. The iron ore preheating is the biggest change compared to the previous diagram. It has been separated into three separate lines. The low temperature section of the iron ore preheating has been moved to the far left of the graph. The second major change is the separation of the ethane reactor into a two-step low and high temperature reaction. This allows a low temperature ethane preheater and reactor to follow the low temperature iron ore preheater. The mid-temperature iron ore preheater follows with the remaining high temperature ethane reactor and iron reactor finishing the diagram. This graph shows that the maximum temperature of the sand line can be reduced by 100°C and still meet the temperature of approach requirements. This improvement could be further extended by continuing to split the reactors and preheaters into ever smaller pieces, and reordering them according to temperature input, but this comes at a price. As the efficiency increases due to a better fit, the complexity of the diagram and potential components also increases. This diagram is believed to be a good balance of efficiency and complexity.

Table 19: Complex Heat Rate vs. Temperature — Q Consumption Breakdown

	%Q Consumed	T low (°C)	T high (°C)	Temperature of approach (°C)
IRONRXN	3.05%	895	895	105 97
HYDPRE+OREPRE2	6.25%	735	895	97 239
ETHCRACK2	40.74%	735	735	239 127
ETHAPRE2	17.05%	535	735	127 281
OREPRE	5.01%	535	735	81 267
ETHCRACK	6.31%	535	535	267 249
ETHAPRE	11.22%	385	535	249 369
OREPRE0	10.37%	25	535	219 700

The exergy analysis of this improved heat rate diagram is shown in Table 20. Due to reducing the maximum temperature of the sand, the exergy stored in the sand is reduced. This reduction accounts for the only change in the overall reduction in the exergy destruction. This is because the same chemical process is still occurring in the second diagram. The second diagram still has the same amount of heat input at exactly the same temperatures. The only difference between the two chemical processes is that it has been segmented to allow for a better fit with the sand line. Overall, the added complexity has allowed a reduction in exergy destruction of about 10%. This reduction will allow for a higher efficiency for the overall cycle in addition to helping alleviate high temperature design requirements.

Table 20: Complex Heat Rate vs. Temperature—Exergy

Component	Q KJ/sec	T effective K	Q exergy KJ/sec
Sand	668342.6	1130.079	492101.7
IRONRXN	20363.8	1193	15277.12
HYDPRE+OREPRE2	41755	1087.711	30315.39
ETHCRACK2	272271	1033	193726.2
ETHAPRE2	113975	906.5311	76508.5
OREPRE	33496.3	906.9926	22490.81
ETHCRACK	42202.2	833	27104.65
ETHAPRE	74986.3	732.2421	44469.18
OREPRE0	69293	527.7383	30165.06
Total	668342.6		440056.9
Exergy Destruction			52044.8

7.3 Comparison with Rankine Cycle Heat Rate vs. Temperature Diagram

A heat rate vs. temperature diagram was also developed for simulating the operation of the combustion chamber for a simple Rankine cycle. This diagram is to compare the proposed chemical production system to the relatively well-developed electricity generating CSHSS being deployed in the American Southwest and in Spain. The diagram simulates using the same CSHSS being developed for the chemical process and instead using it for generating electricity in a Rankine cycle with steam as the working fluid. For the Rankine cycle, constant specific heats were assumed similar to the other diagrams. The cycle includes three main components: a preheater, steam generator and super heater. First, the process starts with 95°C, 50 Bar water. This is heated in the preheater to 264°C, 50 Bar (saturated liquid). The next component of the process is the steam generator. As seen in Table 21, this component consumes approximately 50% of the heat input from the sand. Similar to a conventional superheat Rankine cycle, to prevent erosion from condensing water inside the turbine the steam is superheated to 565°C, 50 Bar. At this point the steam will enter the turbine inlet, generate mechanical work by spinning the turbine, be condensed in a condenser then pumped back to the preheater.

Table 21: Rankine Heat Rate vs. Temperature — Q Consumption Breakdown

Component	%Q Consumed	T low (°C)	T high (°C)	Temperature of approach (°C)
SUPERHEAT	19.34%	264	565	435 683
STEAMGEN	50.60%	264	264	683 544
PREHEAT	30.06%	95	264	544 630

In Figure 15 below, the three components of the Rankine cycle can be seen graph with the same sand line presented in the complex chemical process diagram of Figure 14. It can be observed that the exergy destruction will be significantly higher than that of the two previous diagrams (Figure 13 and 14). This is due to the much large average temperature difference between the sand line and the Rankine process. This shows how the chemical process is a better fit for the use of the high temperature heat as it destroys less potential work. The exergy analysis below gives the quantitative results. Although the chemical process is better than the Rankine cycle, other high temperature applications have also been proposed such as a Brayton Cycle. This would also be a feasible solution to take advantage of the high temperature heat.

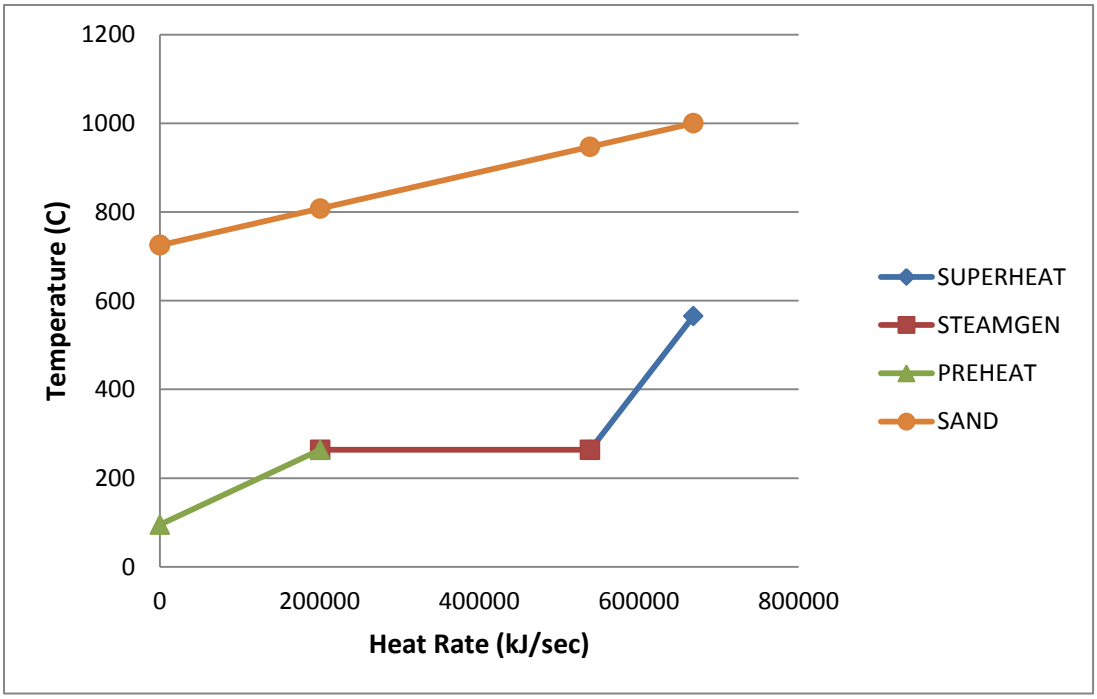

Figure 15: Heat rate vs. temperature diagram for heat exchange between Rankine cycle and sand

The results of the exergy analysis can be seen in Table 22. In this exergy analysis, the Rankine cycle was scaled to have the same total heat input into the steam as was input into the chemical process in Figure 14. This allows the exergy destructions between the two diagrams to be comparable. The Rankine cycle results in a significantly higher exergy destruction of 190 MJ/sec. This is between 3-4 times the exergy destruction of 52 MJ/sec seen in Table 20. This is due to the fact the Rankine cycle runs at much lower temperatures than the chemical process and results in large heat transfer losses.

Table 22: Rankine Heat Rate vs. Temperature—Exergy

Component	Q kJ/sec	T effective K	Q exergy kJ/sec
SAND	668342.6	1130	492101.7
SUPERHEAT	129268.8	679	72527.6
STEAMGEN	338194.9	537	150564.2
PREHEAT	200878.9	487	78057.5
Total	668342.6	0	301149.3
Exergy Destruction			190952.4

8. Conclusion

This thesis seeks to find a viable chemical product application for the high temperature concentrated solar heat. Several chemical production processes were researched to find processes matching solar thermal capability. A coupled iron-ethylene process was proposed as one such application. This process includes the production of ethylene (important in plastics manufacture) from ethane with the byproduct of hydrogen coupled with an iron reduction process that uses the hydrogen as a reducing agent. This iron process would be a completely clean process that would eliminate the use of coal as well as reduce maintenance, pollution, and other draw backs associated with the use of coal. A full analysis of the proposed cycle includes an analysis of the concentrated solar heat supply system's feasibility including an energy payback and economic payback analysis. This analysis was based on designs for a CSHSS being developed at Georgia Tech as well as data produced by NREL's SAM software. The analysis then includes a look at the chemical process. An ASPEN model was created and verified to model the production of iron and ethylene. This model was used to predict the revenue of the iron and ethylene. Research that would be necessary to realize the theoretical cycle was suggested. Next, the analysis includes an exergy analysis of the system. This exergy analysis gives the exergy destruction and stream exergy of each stream verified with multiple methods. Finally, a heat exchanger analysis examined the link between the CSHSS and all of the various chemical processes. Several heat rate vs. temperature diagrams were created for the heat exchange between the sand (thermal storage medium) and the various components in the chemical cycle. This gives a design stage goal for the heat exchanger assuming a 100°C temperature of approach and maximum sand temperature of 1000°C.

Heat from a CSHSS can be used in several industrial chemical processes. The production of hydrogen, quicklime, and metals are all potential products that can utilize the concentrated solar technology. The Iron-Ethylene process has been shown to be a potential production cycle to produce both iron and ethylene using concentrated solar technology. Although plant capital cost estimates are unknown, the production of iron and ethylene yields several hundred times the capital cost of the CSHSS over a plant lifetime of 35 years. This is an indicator that the cycle may be cost effective, if demand for the iron and ethylene products exists. The cycle however has several research challenges that will need to be overcome including the reactor design and membrane separation construction. Because the revenue of ethylene is much greater than that of the iron, the production of iron may not be economically justifiable. Also, due to the lack of growth and specialization of ethylene production, the production of hydrogen may be a more versatile, viable product. The CSHSS feasibility study shows that if the projected costs of the CSHSS can be met, the CSHSS is an economically competitive heat supply system when compared to fuel costs. Positive rates of return were calculated even without including any comparison of a combustion process' capital cost. The energy analysis shows the CSHSS to be one of the best technologies for energy payback. The exergy analysis gives insight into the least efficient processes and which areas will require the most attention in designing an efficient chemical process. One big area of improvement will need to be in finding a use for the large amount of exergy in the ethylene products stream. Finally, the heat exchanger analysis shows that the high temperature chemical process is a much more efficient process than lower temperature Rankine cycles and also gives an example of what the heat exchange between the thermal storage medium of the CSHSS and the various chemical components could look like.

REFERENCES

[1] Sheline W., et al., An Exploratory Study of the Solar Thermal Electrolytic Production of Mg from MgO, Energy. 2013.

[2] Schroeder R., et al., Solar Thermal Electrolytic Process for the Production of Zn from ZnO: The Electrolysis of ZnO from 1275-1500 K. Journal of Solar Energy Engineering. 2011.

[3] Shriver and Atkins. Inorganic Chemistry (Fifth Edition). W. H. Freeman and Company, New York, 2010, pp 383.

[4] Electrolytic extraction of tungsten from western scheelite, J.M. Gomes, University of Michigan 1964

[5] Meier, A., Enrico Bonaldi, et al. Solar chemical reactor technology for industrial production of lime. Solar Power and Chemical Energy Systems Solar PACES 2004

[6] Sheline W., et al. An Exploratory Study of the Solar Thermal Electrolytic Production of Mg from MgO, Energy. 2013.

[7] Larminie James; Andrew Dicks. Fuel Cell systems explained. Wiley and Son 2003

[8] Sheline, W., Said, A., Jeter, S. Concentrated Solar Power Tower: Energy and Economic Feasibility Study. ASME Early Career Technical Journal. American Society of Mechanical Engineers.

[9] Schramek, P., and Maass, J., 2011, “First Heliostat Field Design Calculations for 10 MWth,” Solar Tower Systems confidential report, Munich, Germany.

[10] Al-Ansary, H., Jeter, S., Golob, M., and others, 2011, “Proposed KSU-GIT 10 MWth CRPT SHSS Design,” Georgia Institute of Technology Design, Atlanta, GA.

[11] National Renewable Energy Laboratory, 2011, “Solar Advisor Module Version 2011.12.2”.

[12] Reddy, B.V, and K.S Jagadish, 2003, "Embodied Energy of Common and Alternative Building Materials and Technologies," Energy and Buildings 35, pp. 129-137.

[13] CostWorks: RSMeans. 2008, “Cost Book Data [Data file],” industrial data base, http://www.meanscostworks.com.

[14] McAdams, W. H., 1954, “Heat Transmission, 3rd ed.,” McGraw-Hill, New York.

[15] Meier, P.J., and Kulcinski, G.L., December 2000, “Life-Cycle Energy Cost and Greenhouse Gas Emissions for Gas Turbine Power,” Report no. 202-1. Fusion Technology Institute, University of Wisconsin-Madison.

[16] Meier, P.J., and Kulcinski, G.L., April 2002, “Life-Cycle Energy Cost and Greenhouse Gas Emissions for Building-Integrated Photovoltaics,” Report no. 210-1, Fusion Technology Institute, University of Wisconsin-Madison.

[17] White, S.W., and Kulcinski, G.L, December 1998, “Net Energy Payback and CO2 Emissions from Wind-Generated Electricity in the Midwest,” Report no. UWFDM-1092, Fusion Technology Institute, University of Wisconsin-Madison.

[18] White, S.W., and Kulcinski, G.L, 2000, "Birth to death analysis of the energy payback ratio and CO2 gas emission rates from coal, fission, wind, and DT-fusion electrical power plants," Fusion Engineering and Design, pp. 473-481.

[19] Suzuki, M., and Oka, T., January 1998, “Estimation of life cycle energy consumption and CO2 emission of office buildings in Japan,” Energy and Buildings 28, pp. 33-41.

[20] Dassault Systèmes, 1995-2011, “SolidWorks,” 3D CAD Program.

[21] Falcone, P.K., Noring, J.E., and Hruby, J.M., 1985, “Assessment of a Solid Particle Receiver for a High Temperature Solar Central Receiver System,” Sandia Report SAND85-8208, New Mexico.

[22] Waples, D.W., and Waples, J.S., 2004, “A Review and Evaluation of Specific Heat Capacities of Rocks, Minerals, and Subsurface Fluids: Part 1: Minerals and Nonporous Rocks,” Natural Resources Research, Vol. 13, No. 2, pp.97-122.

[23] Energy Information Administration, 2011, “Electric Power Annual 2010,” Annual Government Information Report, http://www.eia.gov/electricity/annual/pdf/table5.3.pdf

[24] Jeter, S., 2011, “Auxiliary Power Report,” Georgia Institute of Technology, Thermal Energy Systems Lab, internal document.

[25] Sheline, W., 2011, “Investigation of Tower Height and Plant Capacity Correlation”, Georgia Institute of Technology, Thermal Energy Systems Lab, internal document.

[26] Sheline, W., 2012, “Preliminary Test of OLDS Elevator Efficiency”, OLDS Elevator Corporation and Georgia Institute of Technology, Thermal Energy Systems Lab, internal document.

[27] NREL, July 2011, “Levelized Cost of Energy Calculator,” http://www.nrel.gov/analysis/tech_lcoe.html.

[28] Strachan, John; Houser, Richard, 1993, “Testing and Evaluation of Large-Area Heliostats for Solar Thermal Applications” Sandia Report, SAND92-1381.

[29] Hasler, David. 2009, “New Coal-Fired Power Plant Performance and Cost Estimates” Sargent & Lundy LLC, Project 12301-003.

[30] Kolb, G.J., Jones, S.A., et al. 2007, “Heliostat Cost Reduction Study,” Sandia Report, SAND2007-3293.

[31] Energy Information Administration, 2012, “Data Highlights: Natural gas futures price, Crude oil futures price,” Annual Government Information Report, http://www.eia.gov/

[32] California Energy Commission, 2012, “Ivanpah Solar Electric Generating System,” General Description of Project, http://www.energy.ca.gov/sitingcases/ivanpah/index.html.

[33] Chatterjee, A. “Sponge Iron Production by Direct Reduction of Iron Oxide.” PHI Learning Private Limited. 2010.

[34] Chatterjee, A., “Sponge Iron Production by Direct Reduction of Iron Oxide.” PHI Learning Private Limited. 2010.

[35] Argonne National Laboratory“Hydrogen Transport Membrane(HTM) for Separation of Pure Hydrogen at High Temperatures” www.anl.gov/techtransfer/pdf/HTM_RandD.pdf. Accessed April 2013.

[36] Peters, Max; Klaus Timmerhaus, Ronald West, 2002. “Plant Design and Economics for Chemical Engineers” 5th edition. McGraw-Hill Science

[37] Lemos, William. “US spot ethylene plummets 10% amid cracker restart talks,” ICIS, http://www.icis.com/Articles/2012/04/10/9548907/us-spot-ethylene-plummets-10-amid-cracker-restart-talks.html

[38] Energy Information Administration, 2012, “Comparative spot price movements in natural gas, crude oil, and NGLs,” http://www.eia.gov/todayinenergy/detail.cfm?id=1170

[39] Sachs, Janet. “Metal Prices in the United States through 1998,” National Technical Information Service. Revision of PB97-120794INZ.

[40] Chaturvedi, Saurabh. “India Iron Ore Exports May Slump on Mining Ban,” The Wall Street Journal. March 2013. http://online.wsj.com/article/SB10001424127887324685104578388084226800260.html.

[41] Wark, K., Advanced Thermodynamics for Engineers. 1995, McGraw Hill,

[42] Chase, M. Jr., NIST-JANAF Thermochemical Tables Fourth Edition, Journal of Physical and Chemical Reference Data